

**Title:** Low variability runoff inhibits coupling of climate, tectonics, and topography in the Greater Caucasus

---

This manuscript has been submitted for publication in *Earth and Planetary Science Letters*. This version has been revised twice in response to peer review, but is still currently under review and subsequent versions of this manuscript may have slightly different content. If accepted, the final version of this manuscript will be accessible via the “Peer-reviewed Publication DOI” link on the right-hand side of this webpage. Please feel free to contact the authors, we welcome feedback.

---

**Author and Affiliations:**

Adam M. Forte<sup>1</sup>, Joel S. Leonard<sup>2</sup>, Matthew W. Rossi<sup>3</sup>, Kelin X. Whipple<sup>2</sup>, Arjun M. Heimsath<sup>2</sup>, Lasha Sukhishvili<sup>4</sup>, Tea Godoladze<sup>4</sup>, Fakhraddin Kadirov<sup>5</sup>

<sup>1</sup>Department of Geology & Geophysics, Louisiana State University, Baton Rouge, LA, USA

<sup>2</sup>School of Earth and Space Exploration, Arizona State University, Tempe, AZ, USA

<sup>3</sup>Earth Lab, Cooperative Institute for Research in Environmental Sciences (CIRES), University of Colorado, Boulder, CO, USA

<sup>4</sup>Institute of Earth Sciences and National Seismic Monitoring Center, Ilia State University, Tbilisi, Georgia

<sup>5</sup>Institute of Geology and Geophysics of Azerbaijan National Academy of Sciences, Baku, Azerbaijan

Corresponding Author: Adam M. Forte ([aforte8@lsu.edu](mailto:aforte8@lsu.edu))

ORCID ID: 0000-0003-4515-7792

Twitter Handle: @AdamForte83

# 1 **Low variability runoff inhibits coupling of climate, tectonics, and topography in** 2 **the Greater Caucasus**

3  
4 Adam M. Forte<sup>1</sup>, Joel S. Leonard<sup>2</sup>, Matthew W. Rossi<sup>3</sup>, Kelin X. Whipple<sup>2</sup>, Arjun M.  
5 Heimsath<sup>2</sup>, Lasha Sukhishvili<sup>4</sup>, Tea Godoladze<sup>4</sup>, Fakhraddin Kadirov<sup>5</sup>

6  
7 <sup>1</sup>Department of Geology & Geophysics, Louisiana State University, Baton Rouge, LA,  
8 USA

9 <sup>2</sup>School of Earth and Space Exploration, Arizona State University, Tempe, AZ, USA

10 <sup>3</sup>Earth Lab, Cooperative Institute for Research in Environmental Sciences (CIRES),  
11 University of Colorado, Boulder, CO, USA

12 <sup>4</sup>Institute of Earth Sciences and National Seismic Monitoring Center, Ilia State  
13 University, Tbilisi, Georgia

14 <sup>5</sup>Institute of Geology and Geophysics of Azerbaijan National Academy of Sciences,  
15 Baku, Azerbaijan

16  
17 Corresponding Author: Adam M. Forte ([aforte8@lsu.edu](mailto:aforte8@lsu.edu))

## 18 **Highlights**

- 19 • Large, new cosmogenic dataset from the Greater Caucasus
- 20 • Channel steepness index sublinearly varies with erosion rates
- 21 • Stochastic-threshold incision model explains erosion-steepness relationship
- 22 • Nonlinearity interpreted to reflect orographic controls on snowmelt runoff
- 23 • Precipitation phase may modulate degree of climate-tectonic coupling possible

## 24 **Abstract**

25  
26 Hypothesized feedbacks between climate and tectonics are mediated by the  
27 relationship between topography and long-term erosion rates. While many studies show  
28 monotonic relationships between channel steepness and erosion rates, the degree of  
29 nonlinearity in this relationship varies by landscape. Mechanistically explaining controls  
30 on this relationship in natural settings is critical because highly nonlinear relationships  
31 imply low sensitivity between climate and tectonics. To this end, we present a  
32 coordinated analysis of cosmogenic <sup>10</sup>Be concentrations in river sands paired with  
33 topographic, hydroclimatic, and tectonic data for the Greater Caucasus Mountains  
34 where topography is invariant along-strike despite large gradients in modern  
35 precipitation and convergence rates. We show that spatial patterns in erosion rates  
36 largely reflect regional tectonics with little sensitivity to mean precipitation or runoff. The  
37 nonlinearity in the erosion rate – steepness relationship may arise from very low runoff  
38 variability, which we attribute to the large contribution from snowmelt. Transitioning from  
39  
40

41 rainfall- to snowmelt-driven runoff as mean elevation increases is common to many mid-  
42 latitude mountain ranges. The associated decrease in runoff variability may represent  
43 important, unrecognized dynamics inhibiting the sensitivity of tectonics to climate more  
44 broadly.

45

## 46 **1. Motivation**

47 The potential for dynamic coupling between climate and tectonics has driven  
48 decades of research. However, empirical data are equivocal with results both  
49 supporting and rejecting two-way coupling (Whipple, 2009). The extent to which climate  
50 can influence tectonics in fluvial landscapes depends on how climate influences erosion  
51 rates which, in turn, drives the tectonic response to the redistribution of mass in the  
52 lithosphere (Willett, 1999). If the response of topography to increasing uplift and erosion  
53 rates is sublinear, then large changes in rates can only drive slight changes in fluvial  
54 relief and the potential for two-way coupling is low (Whipple and Meade, 2004). In this  
55 study, we focus on daily runoff variability, which when paired with a threshold to  
56 incision, strongly influences the form of the topography-erosion rate relationship (e.g.,  
57 DiBiase and Whipple, 2011; Lague, 2014; Lague et al., 2005). Under this view, regions  
58 with extremely low runoff variability should exhibit a highly nonlinear topography-erosion  
59 rate relationship. We examine this expectation in the Greater Caucasus (GC), where  
60 prior work demonstrates a lack of simple climatic or tectonic influences on topography  
61 despite substantial along-strike gradients in both (Forte et al., 2016). We present a  
62 large, new suite of basin-averaged  $^{10}\text{Be}$  erosion rates along with detailed analyses of  
63 topography, tectonics, and hydroclimate to evaluate whether very low runoff variability in  
64 the GC attributed to snowmelt hydrology can explain the apparent disconnect between  
65 climate, tectonics, and topography. We then consider results in the broader context of  
66 how the relative contributions from snowmelt versus rainfall runoff are expected to  
67 change as mountain ranges grow.

68

## 69 **2. Background**

### 70 **2.1 Fluvial Incision Modeling**

71 The rate of bedrock erosion by rivers,  $E$  [L/t], is often estimated using the stream  
72 power incision model (Lague, 2014) (SPIM):

73  
74 
$$E = KA^m S^n \quad (1)$$

75  
76 where  $K$  [ $L^{1-2m}/t$ ] is a constant encapsulating climate and substrate properties,  $A$  [ $L^2$ ] is  
77 drainage area as a proxy for discharge,  $S$  [L/L] is local river slope, and  $m$  and  $n$  are  
78 dimensionless constants related to erosional process, friction relationship, and width  
79 scaling (Lague, 2014). Within this framework, it is useful to consider a normalized metric  
80 of channel steepness that accounts for the expected co-variation of drainage area and  
81 slope. Normalized channel steepness index ( $k_{sn}$  [ $L^{2m/n}$ ]) is an empirical relationship (e.g.,  
82 Kirby and Whipple, 2012) of the form:

83  
84 
$$k_{sn} = A^{\theta_{ref}} S \quad (2)$$

85  
86 where  $\theta_{ref}$  is a dimensionless index describing the concavity of a channel. In the context  
87 of SPIM,  $\theta_{ref}$  is equivalent to  $m/n$  at steady state. Substituting eq. 2 into eq. 1 generates  
88 a direct, if simple, prediction relating long term erosion rates,  $E$ , to the topography of a  
89 landscape as described by  $k_{sn}$  (Kirby and Whipple, 2012; Lague, 2014):

90  
91 
$$k_{sn} = K^{-1/n} E^{1/n} \quad (3)$$

92  
93 At steady state,  $n$  governs the sensitivity of topography to changes in tectonics or  
94 climate whereby high values imply weaker coupling (e.g., Whipple and Meade, 2004).  
95 Globally,  $E$ - $k_{sn}$  relationships vary widely and range from linear to highly sublinear (Harel  
96 et al., 2016; Kirby and Whipple, 2012; Lague, 2014), necessitating consideration of this  
97 relationship at the landscape scale when evaluating potential climate-tectonic coupling.

98 While predictions from SPIM explain a variety of observations (Kirby and  
99 Whipple, 2012), its simplicity impedes interpretation of the shape of  $E$ - $k_{sn}$  relationships.  
100 One promising alternative are models that incorporate event-scale runoff variability with  
101 erosion thresholds, i.e. stochastic threshold incision models (STIM) (Campforts et al.,

102 2020; Deal et al., 2018; DiBiase and Whipple, 2011; Lague et al., 2005; Scherler et al.,  
 103 2017; Tucker, 2004) where the instantaneous incision rate  $I$  is expressed as:

$$104$$

$$105 \quad I = K\bar{R}^m Q^{*\gamma} S^n - \Psi_c \quad (4)$$

$$106$$

107  $\bar{R}$  [L/t] is mean discharge ( $\bar{Q}$  [L<sup>3</sup>/t]) divided by drainage area,  $Q^*$  is daily discharge divided  
 108 by mean daily discharge,  $\gamma$  is the local discharge exponent, and  $\Psi_c$  is a threshold  
 109 parameter that scales with the critical shear stress for incision ( $\tau_c$  [LM<sup>-1</sup>T<sup>-2</sup>]) and  
 110 substrate erodibility ( $k_e$  [L<sup>2.5</sup>T<sup>2</sup>M<sup>-1.5</sup>]). Eq. 4 reduces to eq. 1 for a constant runoff ( $Q^* =$   
 111 1) and zero threshold ( $\Psi_c=0$ ). Under STIM, the long-term erosion rate,  $E$ , is the  
 112 integration of eq. 4 over a distribution of discharges:

$$113$$

$$114 \quad E = \int_{Q_c(k_s)}^{Q_m} I(Q, k_s) pdf(Q) dQ \quad (5)$$

$$115$$

116 where  $Q_c$  is the minimum discharge that exceeds  $\tau_c$ ,  $Q_m$  is the maximum discharge  
 117 considered, and the  $pdf(Q)$  is the probability distribution of discharge. While a variety of  
 118 probability distributions have been used (e.g., Lague et al., 2005; Tucker, 2004)(e.g.,  
 119 Tucker, 2004; Lague et al., 2005), we use here a two parameter Weibull distribution:

$$120$$

$$121 \quad pdf(Q^*; Q_0, c) = \frac{c}{Q_0} \left(\frac{Q^*}{Q_0}\right)^{c-1} e^{-(Q^*/Q_0)^c} \quad (6)$$

$$122$$

123 where  $c$  is a variability parameter describing the shape of the distribution and  $Q_0$  is a  
 124 scale parameter related to the mean of the distribution. Weibull distributions have been  
 125 shown to describe a wide array of observed daily discharge distributions (Rossi et al.,  
 126 2016) and better characterize observations in the GC than the more commonly used  
 127 inverse gamma distribution (Lague, 2014). Application and derivation of the general  
 128 form of STIM is well documented and thus we refer interested readers to prior studies  
 129 (e.g., Campforts et al., 2020; Deal et al., 2018; DiBiase and Whipple, 2011; Lague,  
 130 2014; Lague et al., 2005; Scherler et al., 2017; Tucker, 2004).

131           The conceptual framing for STIM (Lague et al., 2005; Tucker, 2004) was built  
132 around rainfall events that trigger runoff over the span of hours to days. Stochastic  
133 descriptions of streamflow can be similarly built for snowmelt processes, which are  
134 potentially important in our study area, as long as they account for the transient  
135 accumulation and release of snow water (Schaeffli et al., 2013). While there have been  
136 efforts to integrate snowmelt hydrology into the STIM framework (Deal et al., 2018), we  
137 fully recognize that the complex dynamics of long duration, snowmelt hydrographs on  
138 sediment entrainment, deposition, and bedrock erosion (e.g., Johnson et al., 2010) is  
139 not well represented by the probability distribution of flows alone. Nevertheless,  
140 accounting of the probability distribution of flows is a necessary, if not sufficient, step  
141 towards building an erosion law that can account for both rainfall and snowmelt runoff.  
142 By using STIM as a unifying framework, the degree of nonlinearity of the  $E-k_{sn}$   
143 relationship is directly related to watershed hydrology via the variability parameter (Deal  
144 et al., 2018). Settings with lower discharge variability and thus higher values of  $c$  will  
145 exhibit more nonlinear  $E-k_{sn}$  relationships, all other things being equal.

146

## 147 **2.2 Regional Setting**

148           The Greater Caucasus Mountains (GC) represent the northernmost extent of  
149 deformation caused by the Arabia-Eurasia collision. In the central portion of this  
150 collision, the GC are the main locus of shortening since plate reorganization at ~5 Ma  
151 (Allen et al., 2004). While the timing of reorganization coincides with rapid exhumation  
152 throughout the GC (e.g., Avdeev and Niemi, 2011; Vincent et al., 2020), large  
153 uncertainties remain as to the location, rates, and nature of major structures within the  
154 GC (e.g., Cowgill et al., 2016). Since ~1-2 Ma, active shortening largely stepped out  
155 from the range and localized on a series of foreland fold-thrust belts along its northern  
156 and southern flanks. However, uplift is kinematically linked to active shortening via the  
157 geometry of active faults at depth within the main range (e.g., Forte et al., 2014, 2013;  
158 Mosar et al., 2010; Trexler et al., 2020). Modern convergence (Reilinger et al., 2006)  
159 and precipitation (Forte et al., 2016) rates vary by an order-of-magnitude along strike,  
160 with shortening increasing and precipitation decreasing eastward (Fig. 1). While along-  
161 strike patterns in convergence are complex (Fig. S1), we focus on the component

162 accommodated along the southern range front where we collected new samples (Fig.  
163 1). Whether modern geodetic velocities represent long-term convergence rates is  
164 unclear (Forte et al., 2016), though geodetic rates of shortening are at least consistent  
165 with average rates of shortening from the last 1-2 Ma estimated from balanced cross-  
166 sections (Forte et al., 2013; Trexler et al., 2020).

167 Theory suggests that along-strike variations in precipitation and convergence  
168 rates should lead to an eastward increase in mean elevation, local relief, and width  
169 (Whipple and Meade, 2004). This is not observed in the GC and is not explained by  
170 potential confounding factors like glaciation and lithological heterogeneity (Forte et al.,  
171 2016). Instead, despite similar orogenic widths, topography is relatively invariant along-  
172 strike with an across-strike pattern of lower relief flanks and a higher relief core (Forte et  
173 al., 2016) (Fig. 1). Prior studies attributed the across-strike gradient in topography to a  
174 northward increase in uplift rates along the southern flank of the GC with local maxima  
175 near drainage divides (Forte et al., 2015). Forte et al. (2016) also evaluated whether  
176 trends in mean precipitation were masking other important climate gradients (e.g.,  
177 streamflow variability) that might better explain topographic patterns, to no avail. They  
178 concluded that invariant topography along-strike was either due to a: (1) disconnect  
179 between modern tectonics and climate with the longer-term forcing, or (2) complex, co-  
180 varying relationships between the two. However, interpreting topography alone is  
181 fraught, and testing such hypotheses requires careful sampling of erosion rate data  
182 (e.g., DiBiase et al., 2010; Scherler et al., 2014), a key motivation for this study.

183 Prior estimates of exhumation and erosion rates in the GC largely come from  
184 low-temperature thermochronology (e.g., Avdeev and Niemi, 2011; Vincent et al., 2020,  
185 2011) and modern sediment yields and provenance (e.g., Vezzoli et al., 2020).  
186 Thermochronology data, mostly concentrated west of 44°E, suggests older cooling ages  
187 along the lower relief flanks than the higher relief core, patterns that are broadly  
188 reflected in the topography (Forte et al., 2016). Exhumation rates are representative of  
189 the last ~5-10 Ma and suggest rates of ~1000 m Myr<sup>-1</sup> in the core that decrease to <250  
190 m Myr<sup>-1</sup> towards the flanks (Avdeev and Niemi, 2011; Vincent et al., 2020). Over the  
191 modern era, erosion rates inferred from sediment yields and heavy mineral provenance  
192 imply similar average rates and spatial patterns, but with erosion rates near the range

193 core >2000-3000 m Myr<sup>-1</sup> locally (Vezzoli et al., 2020). At the millennial scale, there is  
194 only one published basin-averaged, <sup>10</sup>Be erosion rate from the Inguri river in the  
195 western GC. The 1100 m Myr<sup>-1</sup> rate (Vincent et al., 2011) is comparable to the long-term  
196 and short-term rates, though it averages across significant variations in steepness and  
197 major knickpoints, and is thus hard to relate to topography. Our new dataset seeks to fill  
198 this knowledge gap by reporting a large, new, millennial-scale, <sup>10</sup>Be erosion rate dataset  
199 that systematically samples across gradients in topographic relief and hydroclimate in  
200 the GC.

201

### 202 **3. Methods**

203 To understand how well topography reflects erosion rates, we sampled and  
204 measured cosmogenic <sup>10</sup>Be in quartz river sands (e.g., Bierman and Nichols, 2004)  
205 from 34 carefully selected, locally equilibrated, unglaciated basins (Fig. 1). Sampling  
206 was coordinated with analyses of modern tectonics, topography, and hydrology of rivers  
207 to better assess predictions of SPIM and STIM fluvial erosion laws. Below, we  
208 summarize these methods. Where appropriate, we provide additional detail in the  
209 Supplement, and raw data and algorithms are archived in a GitHub repository.

210

#### 211 **3.1. Characterizing climate, tectonics, and topography**

##### 212 *3.1.1 Modern Precipitation and Streamflow*

213 We use rainfall data from the Tropical Rainfall Measuring Mission (TRMM) 3B42  
214 product (Huffman et al., 2007), and we use basin-averaged standard deviation of mean  
215 monthly snow cover calculated from MODIS MOD10C2 (Hall et al., 2006). The latter  
216 dataset is used as a proxy for snowmelt, whereby high values imply significant variation  
217 in snow cover through the year (i.e., large amount of snowmelt) and low values imply  
218 small variations in snow cover through the year. Data processing of both are described  
219 elsewhere (Forte et al., 2016). Daily records of discharge (converted to runoff by  
220 dividing by drainage area) for the Caucasus region comes from the Global Runoff Data  
221 Centre (GRDC) and was also originally presented elsewhere (Forte et al., 2016). We  
222 reprocess runoff data here to remove basins whose variability may be artificially low due

223 to dams and fit the distribution of discharge more carefully, the procedure for which we  
224 describe in detail below.

225 To better understand patterns in daily runoff variability, we sought to partition  
226 daily flows into annual, seasonal, and event components (Table S1). Baseflow  
227 separation techniques have received much attention (see review by Eckhardt, 2008),  
228 and our methods are akin to the widely used ‘sliding interval’ baseflow separation  
229 method of Sloto & Crouse (1996). However, baseflow separation efforts typically focus  
230 on binary separation of the overland flow component of the hydrograph. Given our  
231 somewhat different objectives, we instead seek to decompose hydrographs into three  
232 components: (1) an event component that includes event-scale overland flow and  
233 subsurface contributions, (2) a seasonal component that includes the lagged release of  
234 snowmelt runoff and autocorrelated series of rainstorms, and (3) slower inter-annual  
235 changes to the water table. To this end, we quantify the inter-annual component using  
236 the 365-day moving minima and the seasonal component using a 31-day moving  
237 minima minus the annual component. The event-driven component is inferred from the  
238 daily flows minus both the seasonal and annual components, thus satisfying the  
239 condition that the three components sum to the total streamflow (Fig. S2). While  
240 drainage area differences will influence the temporal lag of runoff responses to rainfall  
241 or snowmelt inputs, our analysis focuses only on the regularity of flows under uniform  
242 intervals. In much the same way that our estimates of mean runoff and runoff variability  
243 implicitly subsume the role of drainage area, so does our partitioning of the time series  
244 of streamflow. To develop a climatology of daily flows, we also calculated mean daily  
245 runoff as a function of day of year and apply a 31-day moving mean to smooth over the  
246 influence of individual, large events. Similar analyses on mean daily rainfall from TRMM  
247 are only used to determine the timing and magnitude of peak rainfall in the main text,  
248 though full time series are shown in Fig. S3.

249

### 250 *3.1.2 Modern convergence rates*

251 To compare erosion rates to modern convergence rates, we follow prior efforts  
252 which divided GPS velocities into either a Greater Caucasus or Lesser Caucasus  
253 domain (Avdeev and Niemi, 2011; Forte et al., 2014) and calculated average velocities

254 along-strike using a sliding 50-km moving window (Fig. S1). Convergence between the  
255 Lesser and Greater Caucasus is the difference between these velocities along-strike.  
256 Our results are similar to prior estimates (Forte et al., 2014), but incorporate updated  
257 GPS velocities (Sokhadze et al., 2018).

258

### 259 *3.1.3 Topographic metrics*

260 Topographic analyses of individual basins used TopoToolbox (Schwanghart and  
261 Scherler, 2014) and TAK for TopoToolbox (Forte and Whipple, 2019). Specifically, we  
262 relied on 'ProcessRiverBasins' and related tools within TAK to calculate basin-averaged  
263 statistics of topography and climatology. For basin-averaged topographic metrics, we  
264 use the SRTM 30-m DEM and calculated  $k_{sn}$  using a reference concavity of 0.5. While  
265 this reference concavity is appropriate for the GC (e.g., Forte et al., 2016), we tested  
266 whether the observed shape of the relationship between  $k_{sn}$  and  $^{10}\text{Be}$  erosion rate was  
267 sensitive to the choice of reference concavity and found no measurable differences  
268 across a range of concavities from 0.3-0.6 (Fig. S4).

269

### 270 **3.2. Cosmogenic Erosion Rates from Alluvial $^{10}\text{Be}$ Inventories**

271 Prior to field sampling, we vetted basins that appear to be in local topographic  
272 steady-state (i.e., lacking major knickpoints; outside the influence of LGM glaciation) so  
273 that basin-averaged,  $^{10}\text{Be}$  erosion rates can be reliably related to  $k_{sn}$  (Fig. S5). This  
274 motivated the sampling of 76 basins across the southern range front of the Greater  
275 Caucasus. A subset of 47 were processed for erosion rates (Table S2). Low abundance  
276 of quartz and difficulty in processing due to lithology (see discussion in Supplement)  
277 resulted in usable amounts of quartz for 34 samples. For each sample, we selected the  
278 0.25-1 mm size fraction and used a combination of traditional HF and  $\text{HNO}_3$  leaches  
279 and the 'hot phosphoric acid' technique (Mifsud et al., 2013) to isolate and purify quartz.  
280 Samples were spiked with either commercial or custom low-background  $^9\text{Be}$  carrier, Be  
281 was extracted through liquid chromatography, and BeO was analyzed by accelerator  
282 mass spectrometry at PRIME Lab, Purdue University. To convert blank-corrected,  $^{10}\text{Be}$   
283 concentrations into erosion rates, we calculated effective latitude and elevations to  
284 determine basin-averaged  $^{10}\text{Be}$  production rates (Portenga and Bierman, 2011) and

285 calculated erosion rates in v3.0 of the online calculator formerly known as the CRONUS  
286 calculator (Balco et al., 2008). Erosion rates are reported for a time independent scaling  
287 scheme (Stone, 2000). Additional details on site selection, sample processing, and  
288 erosion rate calculations are provided in the Supplement. All relevant parameters  
289 needed to reproduce erosion rates are provided in Table S3.

290 Due to low quartz yields, we also examined the bedrock geology for each basin  
291 (Forte, 2021) to assess the influence of variable quartz sourcing. By recalculating  
292 topographic metrics and erosion rates after removing portions of basins with lithologies  
293 unlikely to provide quartz, we found no meaningful difference in the  $E-k_{sn}$  patterns (Fig.  
294 S6, Table S3). As another test on the potential sensitivity to non-uniform quartz yields,  
295 we also considered the end-member scenarios where we assume that quartz is entirely  
296 sourced from the upper or lower 50% of each basin and recalculated topographic  
297 metrics and erosion rates (Fig. S6, Tables S3). We found negligible differences in  $E-k_{sn}$   
298 patterns - the central conclusions of this work are insensitive to this complication. For all  
299 three cases, recalculated  $E$  generally lies within the uncertainty bounds of  $E$  calculated  
300 assuming equal sourcing from the entire catchment. This suggests that analytical  
301 uncertainty on erosion rates encompasses uncertainty in quartz sourcing in this setting.

302

### 303 **3.3 Numerical Modeling of River Incision**

#### 304 *3.3.1 Parameterization of SPIM*

305 To assess which SPIM parameters best characterize the relationship between  
306 channel steepness and  $^{10}\text{Be}$  erosion rates, we fit eq. 3 to measured  $E$  and  $k_{sn}$  data. To  
307 do this, we linearize eq. 3 using a log-transform and fit the data using the orthogonal  
308 distance regression (ODR) algorithm in SciPy. To estimate ranges of acceptable fits, we  
309 tested both a Monte Carlo (similar to Adams et al., 2020) and a bootstrap method. While  
310 results are comparable, the bootstrap approach produced wider estimates of  
311 uncertainty. As such, we report fits and uncertainties using the bootstrap method as  
312 more conservative estimates. In fitting the data, we excluded data from one basin  
313 whose uncertainty exceeds its mean value (Fig. S7). We also tested the sensitivity of  
314 fits to the two highest erosion rates. While removal of these two rates suggest a lower  $n$ ,  
315 the range of uncertainties inclusive and exclusive of these data substantially overlap

316 (Fig. S7). Given the lack of any meaningful reason to exclude these data, the reported  
317 fits include these two high erosion rate basins.

318

### 319 3.3.2 Parameterization of STIM

320 STIM is a more complex model than SPIM and requires calibration of a larger  
321 number of parameters. Prior studies provide more detailed discussion of the derivation  
322 of STIM and reasonable parameter values (Campforts et al., 2020; Deal et al., 2018;  
323 DiBiase and Whipple, 2011; Lague et al., 2005; Scherler et al., 2017). For this work,  
324 parameter values are summarized in the Supplement and many ( $k_t$ ,  $\omega_a$ ,  $\omega_s$ ,  $\alpha$ ,  $\beta$ ,  $a$ ) are  
325 set to previously used values (e.g., DiBiase and Whipple, 2011). The six parameters we  
326 vary and/or explicitly test in our analysis are;  $\bar{R}$ ,  $c$ ,  $Q_0$ ,  $k_w$ ,  $\tau_c$ , and  $k_e$ , each of which are  
327 described and justified below.

328 Because none of the  $^{10}\text{Be}$  basins are gauged, we generalize runoff parameters in  
329 gauged GRDC basins for attribution. To estimate  $\bar{R}$  in sampled basins, we needed to  
330 relate  $\bar{R}$  (known for gauged basins) with mean precipitation as measured by TRMM  
331 ( $\bar{P}_{\text{TRMM}}$ ) (known for all basins). To do this, we fit a power law relationship between  $\bar{P}_{\text{TRMM}}$   
332 and  $\bar{R}$  in gauged basins (Fig. 2A) and used this relationship to interpolate  $\bar{R}$  for  $^{10}\text{Be}$   
333 basins (Fig. 2B). It is important to note that this regression implies runoff ratios  $> 1$  for  
334 basins with high runoff. We suspect that runoff ratios  $> 1$  are due to the well-known  
335 underestimation of snowfall from TRMM (Wulf et al., 2016). Increased snow fraction is  
336 generally expected to increase average runoff ratios (e.g., Berghuijs et al., 2014), and  
337 the high runoff ratios for basins with high mean runoff are suggestive of an increasing  
338 contribution from snowmelt. However, we cannot quantitatively assess how snow  
339 fraction may covary with mean precipitation given the uncertainty on  $\bar{P}_{\text{TRMM}}$ .

340 Runoff distributions for gauged basins are characterized using the shape ( $c$ ) and  
341 scale ( $Q_0$ ) parameters of the Weibull distribution (eq. 6). In detail, runoff distributions  
342 within the Caucasus are complex and likely represent distinct seasonal components  
343 described by different probability distributions as observed in the Himalaya (e.g.,  
344 Scherler et al., 2017). However, unlike prior attempts to account for this using hybrid  
345 distributions, the seasonality of the Caucasus is more variable spatially and temporally  
346 than monsoonal settings (e.g., Sutcliffe et al., 2008) and thus systematic separation of

347 just two components is untenable. As such, we instead fit a single distribution to each  
348 individual gauged record that minimizes the misfit between: (1) the observed  $\bar{R}$  and  
349 implied  $\bar{R}$  of the distribution fit and (2) the shape of the tail of the observed and fit  
350 distribution. To do this, we first fit exceedance probability distributions on the natural log  
351 linearized right tail of the distribution above a given threshold (Wilson and Toumi, 2005).  
352 By varying this threshold from 1% (rare) to 60% (frequent) daily exceedances, we found  
353 the threshold that minimizes an objective function that weights a normalized sum of the  
354 mean square of the error on the right tail fit and a normalized difference between the  
355 observed and implied  $\bar{R}$  (Fig. S8). We found the best results when we weighted the  
356 difference between the implied and observed mean by 1.5x. Comparing the observed  
357 and implied mean  $\bar{R}$  (Fig. 3C) and the observed and implied runoff for a flow with a 2-  
358 year return interval (as a proxy for how well the tail of the distribution is honored; Fig.  
359 3D) suggests this method is providing a decent description of both mean and tail  
360 statistics.

361 The scaling between channel width and discharge ( $k_w$ ) is an important, and hard  
362 to constrain, hydraulic geometry relationship that strongly influences the shape of the  $E$ -  
363  $k_{sn}$  relationship predicted by STIM (Lague, 2014). Channel width ( $w$ ) is typically related  
364 to discharge ( $Q$ ) using the function:

$$w = k_w Q^{\omega_a} \quad (7)$$

367 where  $\omega_a$  is a constant we set to 0.5. Following DiBiase and Whipple (2011), we set the  
368 value of  $k_w$  to 15 but test its importance by comparing observed channel widths to  
369 predicted widths for both the mean and 2-year flows (Figs. 4, S10). We measure  
370 channel widths for 26 of the 34 sampled basins using satellite imagery and ChanGeom  
371 (Fisher et al., 2013). We were unable to measure channel widths for all basins because  
372 of poor imagery and/or density of tree cover. This analysis suggests that a  $k_w$  of 15  
373 largely encompasses observations and effectively represents a minimum value for  $k_w$ .  
374 Higher values of  $k_w$  imply increasingly nonlinear  $E$ - $k_{sn}$  relationships. As such, setting  
375 this parameter to 15 for all basins ensures that we are not overestimating the degree of  
376 nonlinearity based on potential variations in  $k_w$  (Fig. 4).

378 Both the erosional efficiency ( $k_e$ ) and threshold shear stress ( $\tau_c$ ) control the  
379 magnitude of the threshold parameter ( $\Psi_c$ ) in STIM (eq. 5), neither of which is well  
380 constrained for our setting. Given the need to fix one parameter to calibrate the other,  
381 our goal is to find a single, best-fit value of  $k_e$  that can be used as representative of the  
382 entire erosion rate dataset. As an initial step, we first seek to find meaningful divisions  
383 within the estimated runoff distributions using k-means clustering on the values of  $c$  and  
384  $\bar{R}$  from the gauged basins (Figure 5A). Clustering results suggest there are 4 semi-  
385 distinct hydroclimatic populations within the gauged basins (Fig. 5A, S11). For each  
386 population, we characterize the aggregate  $\bar{R}$ ,  $c$ , and  $Q_0$  in two different ways, either by  
387 arithmetic means or by creating composite discharge records within each cluster and  
388 refitting the composite distribution (for  $c$  and  $Q_0$  only). The results of both are similar and  
389 we use the refit composite values of  $c$  and  $Q_0$  for subsequent components. We then  
390 assess which runoff cluster ungauged basins belong to based on estimated  $\bar{R}$ , the  
391 maximum elevation of the catchments (which is correlated with the shape and scale  
392 parameters, e.g., Fig. 5C), and geographic proximity to gauged basins (Fig. 5D-E).  
393 Within a given cluster, we then fix the distribution parameters  $c$  and  $Q_0$  to the aggregate  
394 values for that cluster, use the estimated  $\bar{R}$  for individual ungauged basins, fix  $\tau_c$  at 45  
395 Pa, and use STIM to find the  $k_e$  for each basin that most closely reproduces measured  $E$   
396 using the known value of  $k_{sn}$  (Fig. 6A). To account for uncertainty in both  $k_{sn}$  and  $E$  for  
397 each basin, we generate a synthetic distribution of 500  $k_{sn}$  and  $E$  values using the mean  
398 and uncertainties of individual basin values of  $k_{sn}$  and  $E$ . We then find a population of  $k_e$   
399 values for each basin such that individual random  $k_{sn}$  values drawn from the synthetic  
400  $k_{sn}$  distribution minimize the misfit between individual random  $E$  values drawn from the  
401 synthetic  $E$  distribution. This produces a distribution of  $k_e$  values for each  $^{10}\text{Be}$  basin.  
402 We use the median  $k_e$  as our best estimate of  $k_e$  for a particular basin and the statistics  
403 of this distribution (i.e., interquartile range) as an estimate for uncertainty on this value.  
404 To represent populations of basins (whole dataset and clusters), we report medians of  
405 best fit  $k_e$  values (Fig. 6A). We also do a similar exercise where we fix  $k_e$  to the median  
406 value from above and estimating  $\tau_c$  values for individual  $^{10}\text{Be}$  basins (Fig. 6B).

407 The approach we take to estimate  $k_e$  (or  $\tau_c$ ) assumes limited influence of  
408 lithology on  $k_e$  or  $\tau_c$ , which is consistent with prior results from the GC (Forte et al.,

2016, 2014) and reinforced by the lack of correlation between the optimized  $k_e$  values and lithology (Fig. S12). While some studies applying STIM to cosmogenic erosion rates use grain size measurement to constrain  $\tau_c$  (DiBiase and Whipple, 2011), the challenge of obtaining such data prompts many studies like ours to assume a reasonable grain size and corresponding  $\tau_c$  (Campforts et al., 2020; Scherler et al., 2017), as we do here.

414

## 4. Results

### 4.1 Relating Erosion Rates to Topography

Erosion rates,  $E$ , vary from 33-5610 m Myr<sup>-1</sup> (Figs. 7). Rates do not simply vary with along-strike position (Fig. S13), but increase monotonically with LC-GC convergence rates (Forte et al., 2014; Kadirov et al., 2012; Reilinger et al., 2006; Sokhadze et al., 2018) (Fig. 7). Across-strike  $E$  systematically increases from the southern flanks of the range towards the core, reaching a peak south of the topographic crest (Fig. 7C). Despite the wide range of  $E$ , all data lie on a single, highly nonlinear relationship between  $k_{sn}$  and  $E$  (Fig. 8A). Similar relationships exist between  $E$  and mean basin slope due to the quasi-linear relationship between  $k_{sn}$  and slope in this setting (Fig. 8C). Remarkably, over erosion rates from ~300 to >5000 m Myr<sup>-1</sup>, channel steepness is essentially invariant, ranging between ~300-500 m (Fig. 8). While there is substantial scatter in these high  $E$  and  $k_{sn}$  basins, this is not unusual for these kinds of datasets and reflects both geologic and analytical uncertainty in the erosion rate estimates and the merging of two distinct  $k_{sn}$ - $E$  relationships associated with catchments in clusters 2 and 3 (30 of 34 data points, Fig. 8A). Moreover, detailed interrogation of potential confounding factors reveals no meaningful way to subdivide these data into different physically interpretable populations (Fig. S14).

433

### 4.2 River Incision Modeling

Fitting data with the SPIM (eq. 3) suggests an  $n$  of 3.1 to 4 with a median value of 3.5 (Fig. 8, Fig. S7). This is in the range of  $n$  found elsewhere, but well above the global mean value of ~2.5 (Harel et al., 2016; Lague, 2014).  $E$  does not systemically vary with  $\bar{P}_{TRMM}$  (Fig. 8B) or  $\bar{R}$  (Fig. 8A). Similarly, while channel narrowing in response to increasing uplift rates can produce a nonlinearity in  $E$ - $k_{sn}$  relationships during

440 transients (e.g., Gallen and Fernández-Blanco, 2021), in the GC there is not a clear  
441 relationship between the wideness of channels and  $k_{sn}$ , suggesting this is not a  
442 significant contributor (Fig. 4C) and consistent with observations in equilibrium  
443 landscapes across a range of uplift rates elsewhere (e.g., Whipple et al., 2022). Given  
444 this outcome, we turn to STIM which explicitly accounts for daily runoff variability, to see  
445 how well it explains the strong nonlinearity in the empirical  $E$ - $k_{sn}$  relationship.

446 Figure 6 shows that optimized  $k_e$  varies over six orders of magnitude, though  
447 most data lies within 1 order of magnitude of the median  $k_e$  (Fig. 6). There is an  
448 apparent relation between position within the range and/or erosion rate (which are  
449 correlated, e.g., Fig. 7C) and  $k_e$  or  $\tau_c$  (Fig. 6). We further consider possible implications  
450 of spatial variations in  $k_e$  or  $\tau_c$  implied from our optimization in the discussion.

451 Within a given cluster, application of STIM using the whole population  $k_e$  and  $\tau_c$   
452 parameters and either the aggregate or individual gauged basins values of  $c$  and  $Q_0$   
453 produces moderate correspondence with the observed  $E$ - $k_{sn}$  relationship within that  
454 cluster (Fig. 9, S15). Ultimately, while the single SPIM relationship provides a suitable fit  
455 to the entire dataset (Fig. 8, S15), the application of the STIM within clusters highlights  
456 that the degree of scatter in the observed  $E$ - $k_{sn}$  may reflect the detailed hydroclimatic  
457 variations within the Caucasus region, facilitating a data-driven interpretation to the  
458 nonlinear relationships observed. In detail, the appearance of a pseudo-maximum  $k_{sn}$ ,  
459 appears to largely result from the mixing of primarily two different, but both sublinear  $E$ -  
460  $k_{sn}$  relationships (i.e., cluster 2 & 3, Fig. 8A).

461

## 462 **5. Discussion**

### 463 **5.1 Tectonic Implications for the Greater Caucasus**

464 Our new cosmogenic erosion rates in the GC are broadly consistent with prior  
465 million-year and decadal rates. All suggest systematic increases in  $E$  toward the core of  
466 the range, with maximum  $E$  greater than 1000-2000 m Myr<sup>-1</sup> (Avdeev and Niemi, 2011;  
467 Vezzoli et al., 2020; Vincent et al., 2020, 2011), though our maximum rates of ~5000 m  
468 Myr<sup>-1</sup> exceed most estimates from thermochronology or sediment yields. The broad  
469 agreement between  $E$  and GC-LC convergence rates suggest that millennial scale  $E$   
470 faithfully records modern tectonic forcing (Fig. 7), which likely reflect average geologic

471 rates of shortening over the last 1-2 Ma (Forte et al., 2013; Trexler et al., 2020). Spatial  
472 patterns in cosmogenic  $E$  are consistent with the expected vertical components of GC-  
473 LC shortening rates applied to north-dipping structures with reasonable dips (Fig. 7D),  
474 though we emphasize that the geometry of structures in the interior of the GC are not  
475 well constrained (e.g., Cowgill et al., 2016; Forte et al., 2014). The across-strike pattern  
476 of increasing  $E$  toward the topographic crest, is consistent with prior suggestions of a  
477 thrust ramp beneath the southeastern range-front (e.g., Forte et al., 2015), but does not  
478 require this geometry. While there is substantial scatter in these spatial relationships,  
479 likely due to local structural complexity, this result strongly contrasts with the poor  
480 correlation between  $E$  and mean rainfall or estimated runoff (Fig. 8). From this, we reject  
481 a simple climatic control on  $E$  in this setting, and the rest of our discussion focuses on  
482 what more careful consideration of hydroclimate reveals.

483

## 484 **5.2 Application of STIM to the Greater Caucasus**

485 The ability of STIM to reproduce observed  $E$ - $k_{sn}$  relationships (Fig. 9) suggests  
486 that the shape of this relationship in the GC is aided by considering the systematic  
487 decrease in runoff variability with elevation (e.g., Fig. 5C). STIM unpacks the bulk  
488 treatment of climate in SPIM by characterizing hydroclimate using a simplified model of  
489 runoff generation ( $Q = R * A$ ) and an assumed probability distribution of daily runoff  
490 (Weibull parameters  $c$  and  $Q_0$ , which are genetically related to the empirical mean). The  
491 k-means cluster analysis suggests at least four distinct hydroclimatic regimes in the  
492 Caucasus (Fig. 5, S11). Specifically, we find clusters generally correspond to high runoff  
493 and higher variability (Cluster 1:  $\bar{R} > 4$ ,  $c < 1$ ), high runoff and lower variability (Cluster  
494 1:  $\bar{R} > 4$ ,  $c > 1$ ), low runoff and higher variability (Cluster 2:  $\bar{R} < 4$ ,  $c < 0.9$ ), and low  
495 runoff and lower variability (Cluster 3:  $\bar{R} < 4$ ,  $c > 0.9$ ). These clusters also have clear  
496 spatial relationships, with a general trend of basins with higher maximum elevations  
497 corresponding to lower daily runoff variability (Fig. 5C).

498 Cluster analysis allows us to evaluate model performance in terms of broad  
499 variations in hydroclimate. In general, model parameters derived from gauged basins  
500 improves  $E$ - $k_{sn}$  predictions for ungauged basins (Fig. 9). This is especially true for  
501 Cluster 2, which includes the bulk of the erosion rate basins, but also performs

502 acceptably for Cluster 3, despite the apparent mismatch between the imposed  $k_e$  and  
503 the ranges of  $k_e$  for Cluster 3 basins (Fig. 6). The high runoff clusters 1 and 4 do not  
504 perform as well with only 1 of the 4 basins being well explained by the model. Given that  
505 none of the other 3 basins are clear outliers in the overall  $E$ - $k_{sn}$  relationship (Fig. 8A) or  
506 relationships between  $E$  and convergence velocity (Fig. 7D), we interpret the mismatch  
507 to be due to anomalously high  $k_{sn}$  in these basins. Lithological differences do not  
508 explain these anomalously steep basins (e.g., Fig. S16) indicating that other model  
509 parameters must differ for these basins and/or vary systematically with runoff. It is  
510 important to note here that the boundaries between clusters appear gradational (Fig.  
511 5C). Thus, the extent to which individual basins are not well explained by predicted  $E$ -  
512  $k_{sn}$  relationships could in part reflect either (1) incorrect cluster membership or (2) that  
513 the true range of discharge distributions are not represented by the admittedly small  
514 number of gauged basins.

515 The observed mismatches within clusters could also reflect real variability in  $k_e$ ,  
516 which we impose as a constant. Optimization of  $k_e$  results suggest that rock erodibility  
517 increases (or incision thresholds decrease) towards the center of the range (Fig. 6). If  
518 real, it could imply a systematic weakening of rocks (or decrease in mean grain sizes)  
519 toward the core of the orogen. This could be indicative of more fractured rocks due to  
520 periglacial processes or accumulated tectonic damage. There also exists a weak  
521 positive correlation between optimized  $k_e$  and erosion rate (Fig. 6), which is cross  
522 correlated with distance from the center of the range (Fig. 7C). Systematic variations of  
523 incision thresholds with increasing erosion rate have been suggested (Shobe et al.,  
524 2018), but are thought to operate in the opposite direction whereby more rapid uplift  
525 leads to coarser material and less erodible channels. However, the apparent variability  
526 within  $k_e$  may also be an artifact of discrete clustering of data that reflect a continuum  
527 of behavior. For example, clusters 2 and 3 overlap. Use of cluster 2 parameters for  
528 cluster 3 largely erases cross-correlations among optimized  $k_e$ , erosion rate, and  
529 proximity to the core of the range, begging caution in interpreting these findings.  
530 Interpretation of these patterns requires detailed observations of rock properties and  
531 grain size distribution to provide an additional constraint. Regardless of the challenge of  
532 determining which set of parameters are 'most representative,' the utility of the cluster

533 analysis is that it highlights that the range of scatter observed in the  $E-k_{sn}$  relationship  
534 should be expected for the range of hydroclimatic variability observed in this setting.  
535 Furthermore, sub-dividing by these hydroclimatic domains reveal that (1) runoff  
536 distributions are all strongly sublinear and (2) the sublinear nature of the observed  $E-k_{sn}$   
537 relationship in aggregate reflects mixing of a suite of different sublinear relationships,  
538 which is dominated by contributions from cluster 2 and 3 (Fig. 8A, 9).

539 To further probe the  $E-k_{sn}$  relationship, we attempt to relate the clusters to their  
540 underlying hydroclimatology. Figure 10A shows smoothed mean daily runoffs as a  
541 function of time of year. In general, we interpret the strong seasonal signals in the GC  
542 as indicative of a dominant component of snowmelt runoff, especially when maxima  
543 occur in the spring or summer, though this could reflect other sources (e.g., where  
544 seasonal rainfall is correlated with seasonal streamflow). This is consistent with prior  
545 observations in the GC highlighting the importance of spring and summer snowmelt in  
546 the hydrology of the range (e.g., Kuchment et al., 2010; Rets et al., 2018; Verdiev,  
547 2009). Snowmelt contributions contribute up to 50% of the runoff during the summer  
548 months in high elevation catchments (e.g., Vasil'chuk et al., 2016). For high mean  
549 runoffs, both cluster 1 and 4 basins show a strong seasonal signal that is systematically  
550 offset from peak precipitation. While cluster 4 generally has a single high runoff mode in  
551 the GC, cluster 1 appears more complex with multi-modal seasonality. At lower mean  
552 runoff, cluster 2 basins exhibit muted to non-existent seasonality in runoff and less  
553 systematic relations to the timing of peak rainfall. Cluster 3 basins show clear  
554 seasonality with a dominant peak in runoff in the late spring and early summer. This  
555 peak in runoff occurs shortly after a peak in rainfall, also in the late spring, but there is a  
556 noticeable peak in the late fall with no corresponding runoff peak which we attribute to  
557 the building of a snowpack (Fig. S3). Regardless of cluster, higher elevation basins  
558 typically show summer seasonality, reinforcing our interpretation that snowmelt is the  
559 dominant driver of seasonal flows throughout the Caucasus region (Fig. 10A).

560 Figure 10A does not fully characterize the regularity of flows because data were  
561 smoothed to develop a seasonal climatology. To probe whether and how well  
562 streamflow seasonality explains the runoff variability parameter,  $c$ , we also partitioned  
563 time series data into three components: event, seasonal, and annual fractions which

564 together sum to the total water flux. For gauged basins, the seasonal component shows  
565 a positive correlation with runoff variability (shape), especially for basins in the GC (Fig.  
566 10B). Similarly, the shape and scale parameters exhibit a strong negative correlation  
567 with the event component (Fig. S17). Given that we attribute the seasonal component to  
568 spring/summer snowmelt with modest contributions from seasonal rainfall in some  
569 basins, we interpret patterns in runoff variability to be principally driven by the  
570 contribution of snowmelt to runoff. This is reinforced with the observed positive  
571 relationship between daily runoff variability (shape) and basin-averaged standard  
572 deviation of mean monthly snow cover, a metric used by Forte et al., (2016) as a proxy  
573 for snowmelt (Fig. 10C). We thus interpret our STIM results to at least partially account  
574 for orographic patterns in runoff variability that embed the long hydrologic response  
575 times associated with snowmelt runoff (Deal et al., 2018).

576

### 577 **5.3 Implications for Interactions Among Climate, Tectonics, and Topography**

578 The nonlinearity of the  $E-k_{sn}$  relationship in the GC explains why prior work (Forte  
579 et al., 2016) failed to recognize the influence of either precipitation or convergence  
580 gradients in the topography of the range (e.g., Fig. 1). Such a relationship predicts  
581 relatively invariant  $k_{sn}$  at high erosion rates. Millennial scale erosion patterns are also  
582 concordant with convergence rates and proximity to the core of the range (Fig. 7).  
583 Higher rates near the core of the range are similar to patterns observed in both  
584 sediment flux estimates (Vezzoli et al., 2020, 2014) and bedrock thermochronology  
585 (Avdeev and Niemi, 2011; Vincent et al., 2020), suggesting this reflects a fundamental  
586 detail of the orogen's architecture. The similar width of the range along-strike (Forte et  
587 al., 2014) (Fig. 1) and the low sensitivity of channel steepness to  $E$  exceeding 300-500  
588 m Myr<sup>-1</sup> (Fig. 8A) explains why topography (e.g., mean elevation and local relief) is  
589 relatively invariant along-strike. STIM helps reconcile apparently large contrasts in mean  
590 annual precipitation and runoff between basins (Fig. 8B) by only considering the role of  
591 flows above the incision threshold. While we recognize that the simplistic representation  
592 of events in STIM does not fully capture seasonal dynamics in the GC (e.g., Fig. 9,10,  
593 S3,S9), the general result that low variability runoff leads to highly nonlinear  $E-k_{sn}$   
594 relationships (DiBiase and Whipple, 2011; Lague, 2014; Lague et al., 2005) coupled

595 with the mixing of primarily two different, but both sublinear  $E-k_{sn}$  relationships provides  
596 a satisfying explanation for the pseudo-threshold- $k_{sn}$  behavior (e.g., Fig. 8, 9) and the  
597 lack of a clear climate signal in the topography.

598         While significant uncertainties remain, we consider the most likely explanation to  
599 be one where the orographic patterns in variability and the nonlinearity of the  $E-k_{sn}$   
600 relationship relate to the importance of snowmelt. This is consistent with previous work  
601 probing seasonal patterns of runoff in the GC (e.g., Kuchment et al., 2010; Rets et al.,  
602 2018; Vasil'chuk et al., 2016; Verdiev, 2009) and the more general observation that  
603 mountain regions with a large snow fraction tend to have lower event-scale runoff  
604 variability (e.g., Rossi et al., 2016) as the dominant flood generating mechanism  
605 changes from rainfall to snowmelt runoff (e.g., Berghuijs et al., 2016). If correct, our  
606 hypothesized link between the nonlinearity in the  $E-k_{sn}$  relation and low variability  
607 snowmelt runoff has interesting implications. Under modern climate, only tributary  
608 basins on the low elevation and low erosion rate flanks of the range should be  
609 topographically sensitive to either climatic or tectonic changes. These areas: (1) have  
610 higher runoff variability due to a lesser influence of snowmelt (Fig. 5, 10), and (2) are in  
611 the quasi-linear portion of the  $E-k_{sn}$  relationship (Fig. 8). Conventional approaches  
612 toward accounting for orographic precipitation in landscape evolution have focused on  
613 elevation-dependent mean annual rainfall (Bookhagen and Burbank, 2006) or snowfall  
614 (Anders et al., 2008). This work highlights the critical role of the transition from rainfall-  
615 to snowmelt- driven hydrology in mediating runoff variability itself (Rossi et al., 2020), an  
616 important complexity rarely considered in landscape evolution studies. Transitioning  
617 from rainfall- to snowmelt- driven hydrology is dictated by the elevation distribution  
618 within a mountain range and presents a possible direct relation between climate and  
619 erosion rates in orogenic systems, albeit not in the traditional sense where there is a  
620 positive correlation between erosion and precipitation or runoff rates (Ferrier et al.,  
621 2013) . Importantly, a snowmelt control on runoff variability may be relevant to many  
622 mountain ranges where the growth of topographic relief has undermined the erosive  
623 ability of higher mean annual precipitation by distributing flows over longer duration  
624 snowmelt events.

625

626 **6. Conclusions**

627 We present a large suite of new basin-averaged  $^{10}\text{Be}$  erosion rates from the  
628 Greater Caucasus that are consistent with longer term exhumation and shorter-term  
629 decadal scale rates. Erosion systematically varies with convergence rates between the  
630 Greater Caucasus and Lesser Caucasus and is uncorrelated to mean annual rainfall,  
631 favoring a tectonic control on erosion rates. The relationship between erosion and  
632 channel steepness is extremely nonlinear in this setting. However, consideration of  
633 regional hydro-climatology incorporated into a stochastic threshold incision model of  
634 river incision suggests that low variability, snowmelt runoff may drive this nonlinearity,  
635 thus explaining why prior efforts failed to recognize a clear climatic imprint on  
636 topography in the mountain range.

637 Our results also highlight the importance of both: (1) considering regionally  
638 constrained relationships between topography and erosion when assessing potential  
639 climate-tectonic interactions, and (2) endeavoring to understand the underlying  
640 mechanism(s) setting that form. In the Greater Caucasus, significant climate-tectonic  
641 interactions are precluded because topography becomes insensitive to changes in  
642 forcing at uplift rates exceeding  $300\text{-}500\text{ m Myr}^{-1}$ . This contrasts with settings where  
643 relationships between erosion and topography may be more linear. We emphasize that  
644 the observed nonlinearity between erosion rates and channel steepness in the GC is  
645 not a global solution to an apparent lack of coupling between climate and tectonics.  
646 Rather, the wide range of such relationships around the world likely reflects important  
647 landscape specific, hydro-climatic details that must be considered when applying  
648 erosion models. Our results also show that spatial and temporal patterns in precipitation  
649 phase that alter flood frequency may be an underappreciated governor on the degree of  
650 climate-tectonic coupling possible in mid-latitude mountain ranges not heavily  
651 influenced by glacial erosion.

652

653 **Acknowledgements**

654 This work was supported by the National Science Foundation grant EAR-1450970 to  
655 A.M.F. and K.X.W. We thank Charles Trexler and Alexander Tye for collecting a small  
656 subset of the samples used in this analysis; Eric Cowgill and Nathan Niemi for help and

657 advice related to this project both in and out of the field; Dachi Injia, Giga Ugrekheldze,  
658 Davit Kapanadze, and Zurab Javakhishvili for assistance in the field; and Byron Adams  
659 and Roman DiBiase for helpful discussions and sharing codes. We acknowledge the  
660 GRDC for providing runoff data, available here  
661 ([https://www.bafg.de/GRDC/EN/Home/homepage\\_node.html](https://www.bafg.de/GRDC/EN/Home/homepage_node.html)). We thank editor Jean-  
662 Philippe Avouac and reviewers Dirk Scherler and Jane Willenbring for comments which  
663 improved this manuscript. We also thank two anonymous reviewers of an earlier draft of  
664 this manuscript.

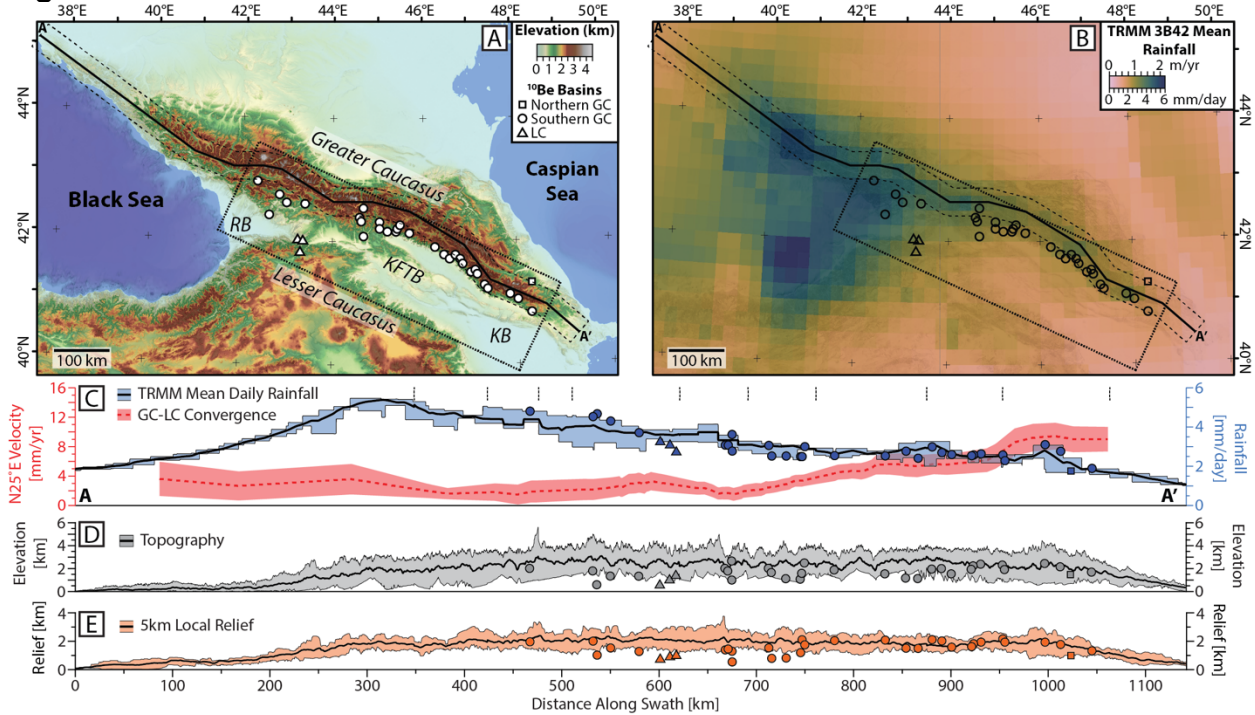
665

### 666 **Data Availability**

667 The authors certify that all data necessary to reproduce the key findings of this paper  
668 are presented in the manuscript or its supplement. We additionally provide the majority  
669 of the data tables as plain text, shapefiles of the  $^{10}\text{Be}$  basins, the GRDC basins, some  
670 select rasters that are generally not easily available, and many of the analysis scripts in  
671 a GitHub repository ([https://github.com/amforte/Caucasus Erosion](https://github.com/amforte/Caucasus_Erosion); DOI:  
672 10.5281/zenodo.6353857). The lithologic compilations are provided as a separate open  
673 access permanent repository (Forte, 2021: <https://doi.org/10.5281/zenodo.5752511>).

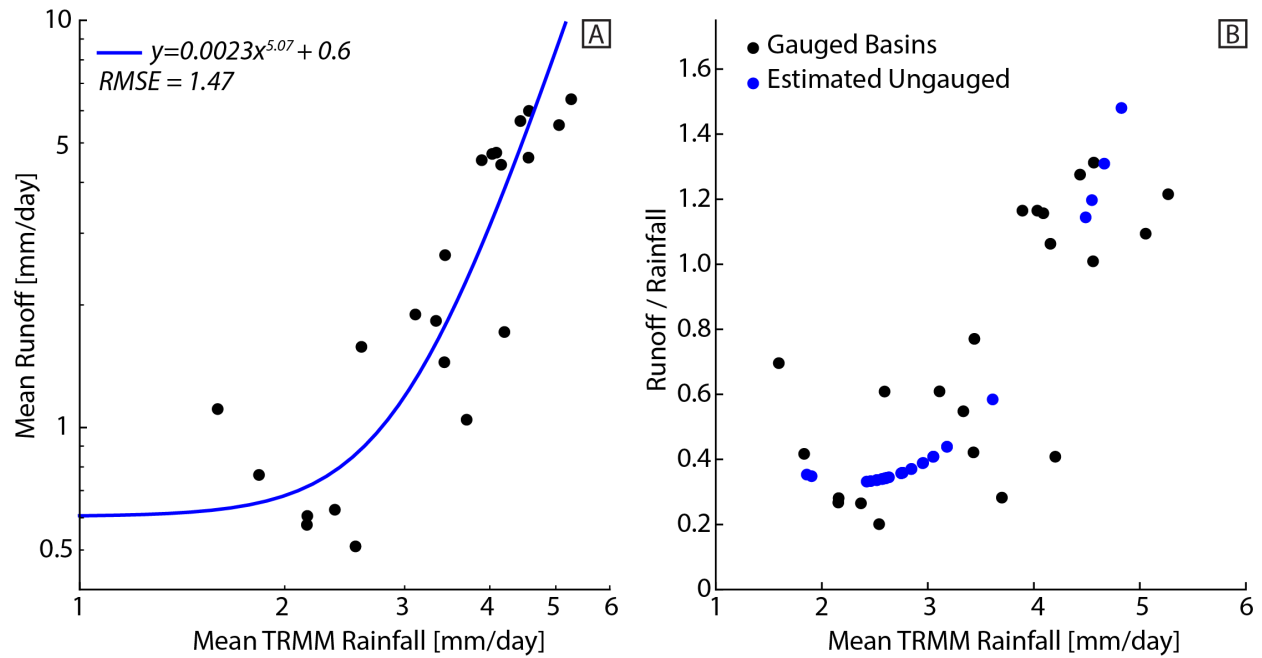
674  
675

## Figures



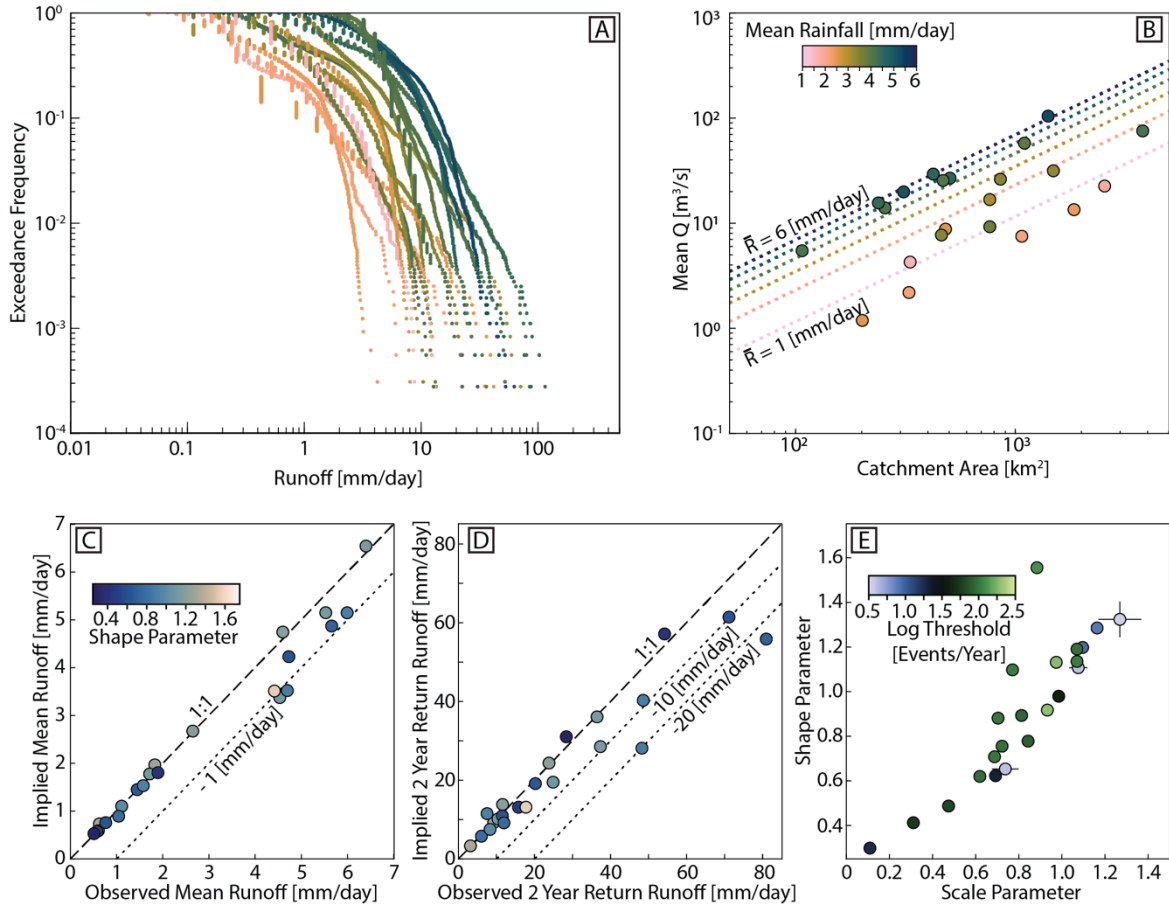
676  
677

678 **Fig 1.** (A) Regional map with location of alluvial cosmogenic  $^{10}\text{Be}$  samples (white  
679 symbols) within the Greater and Lesser Caucasus (LC). Line A-A' and corresponding  
680 box outline 50-km wide swath referenced in other figures and is centered on the  
681 topographic crest of the range. Dotted rectangle is outline of Fig 7A. KFTB – Kura Fold  
682 Thrust Belt, KB – Kura Basin, RB – Rioni Basin. (B) TRMM 3B42 mean daily rainfall  
683 (Forte et al., 2016). (C) Blue shaded region is maximum and minimum rainfall within the  
684 swath in panel B (line is mean value). Blue symbols are mean rainfall in sampled  
685 basins. Red shaded region is estimated convergence rates between the Greater and  
686 Lesser Caucasus along the southern margin of the Greater Caucasus, and is largely  
687 similar to that calculated by Forte et al., (2014). It was recalculated to include more  
688 recent GPS data (see Supplement and Fig. S1). (D) Swath of topography. Symbols are  
689 mean elevation within sampled basins. (E) Swath of local relief using a 5-km radius  
690 circular moving window. Symbols are mean relief within sampled basins.



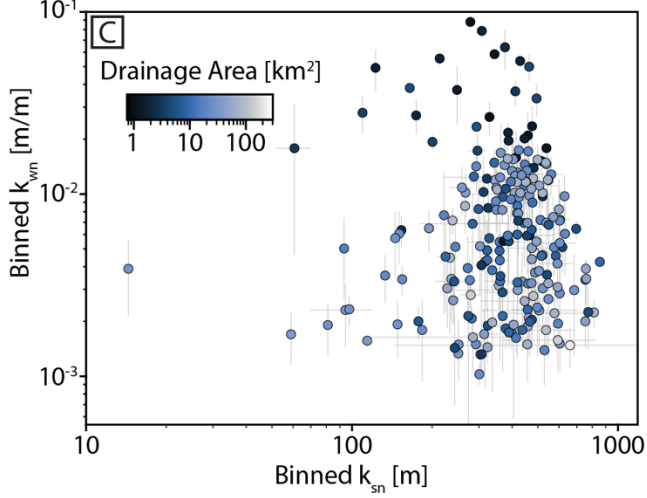
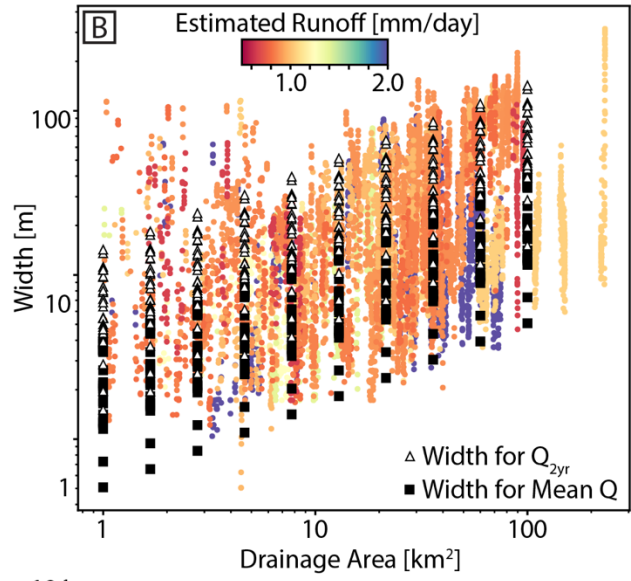
691  
 692  
 693  
 694  
 695  
 696  
 697  
 698  
 699  
 700  
 701

**Fig 2.** (A) Relationship between mean TRMM rainfall within gauged GRDC basins and mean runoff used to estimate runoff in ungauged basins from mean TRMM rainfall. (B) Comparison between mean TRMM rainfall and implied runoff ratio for both the gauged basins and the ungauged basins. Note that both in the gauged and ungauged basins, runoff ratios exceed 1 at high rainfall (runoff) rates. This likely implies an underestimation of TRMM rainfall, e.g., from missing snowfall (Wulf et al., 2016), as opposed to a real runoff ratio which exceeds 1.



702  
703  
704  
705  
706  
707  
708  
709  
710  
711  
712  
713  
714  
715  
716  
717  
718  
719  
720

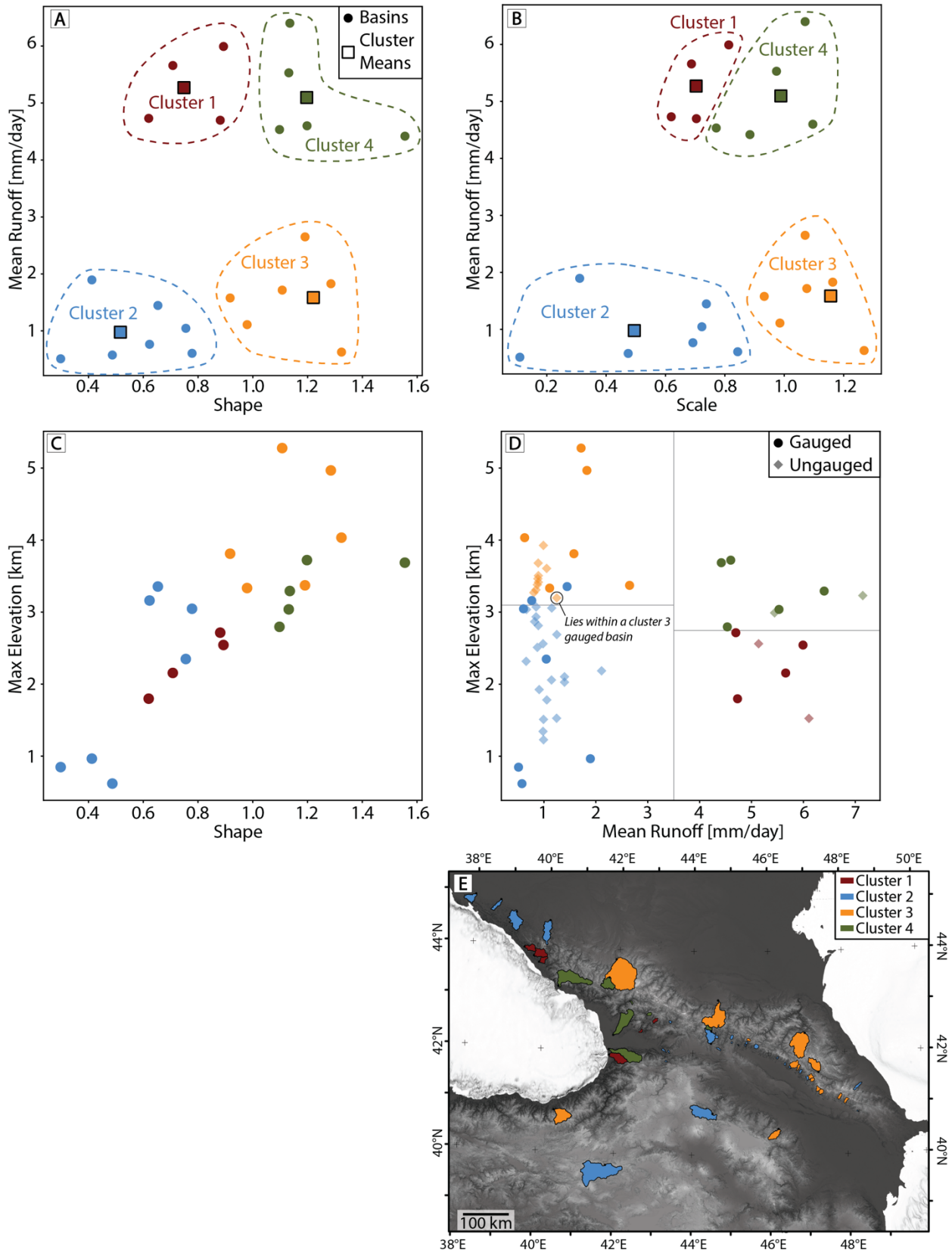
**Fig 3.** (A) Exceedance frequency versus daily runoff for each GRDC basin and colored by mean rainfall estimated from TRMM 3B42. Runoff calculations assume a linear scaling with drainage area, see 3B. (B) Mean discharge versus drainage area colored by mean rainfall for each GRDC basin. The quasi-linear relationship between discharge and drainage area, after parsing by mean rainfall, is consistent with a linear scaling of runoff ( $\bar{Q} = \bar{R}A$ ). Lines represent constant mean runoff assuming this linear scaling. (C) Comparison of observed mean runoff and that implied by the fitting of the individual gauged basin discharge distributions with a Weibull (stretched exponential) distribution, see text for details. (D) Comparison of observed and implied 2-year return flood runoff magnitudes from the fitting of the distributions (E) Comparison of shape and scale parameters resultant from the fits. Dots are scaled by the threshold (i.e., average number of events per year that define the tail of the distribution) that yielded the best fit for individual basins. Fig. S8 provides an example of the fitting technique we use and Fig. S9 compares the results of our preferred fitting technique and a fit of the whole distribution via the method of moments.



721  
722  
723  
724

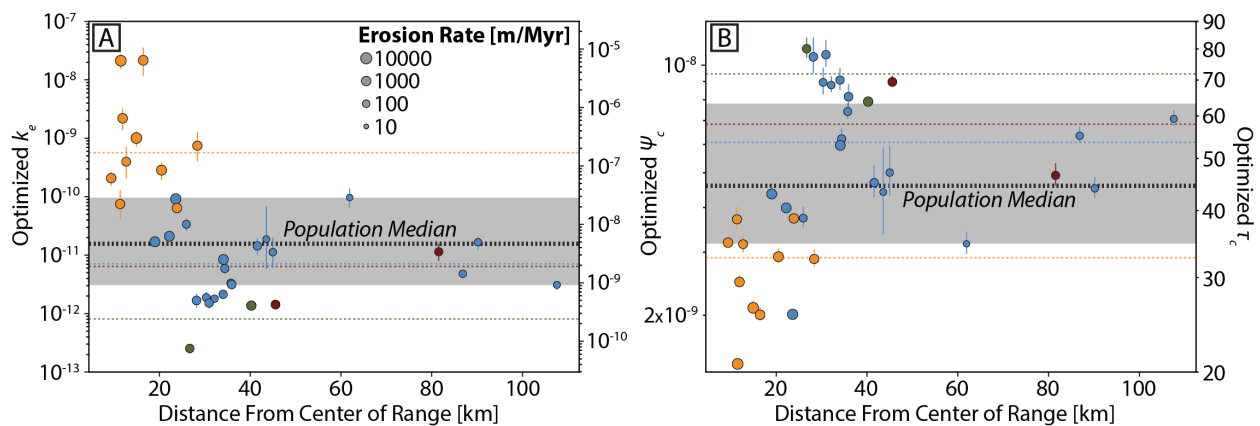
**Fig 4.** (A) Example of channel width as measured on satellite imagery from Google Earth using ChanGeom (Fisher et al., 2013). (B) Measured widths (dots colored by estimated runoff of each basin) and predicted widths using  $k_w = 15$  and either the mean

725 discharge or the 2-year flood (black symbols) as a function of drainage area. Additional  
726 comparisons between width and drainage area scaling are provided in Fig. S10. (C)  
727 Comparison of mean wideness ( $k_{wn}$ ) to mean  $k_{sn}$  within 1 km segments, colored by the  
728 maximum drainage area of the same segments. Wideness is calculated as discussed in  
729 Lague (2014), i.e.,  $k_{wn} = wA^{-0.5}$ .  
730



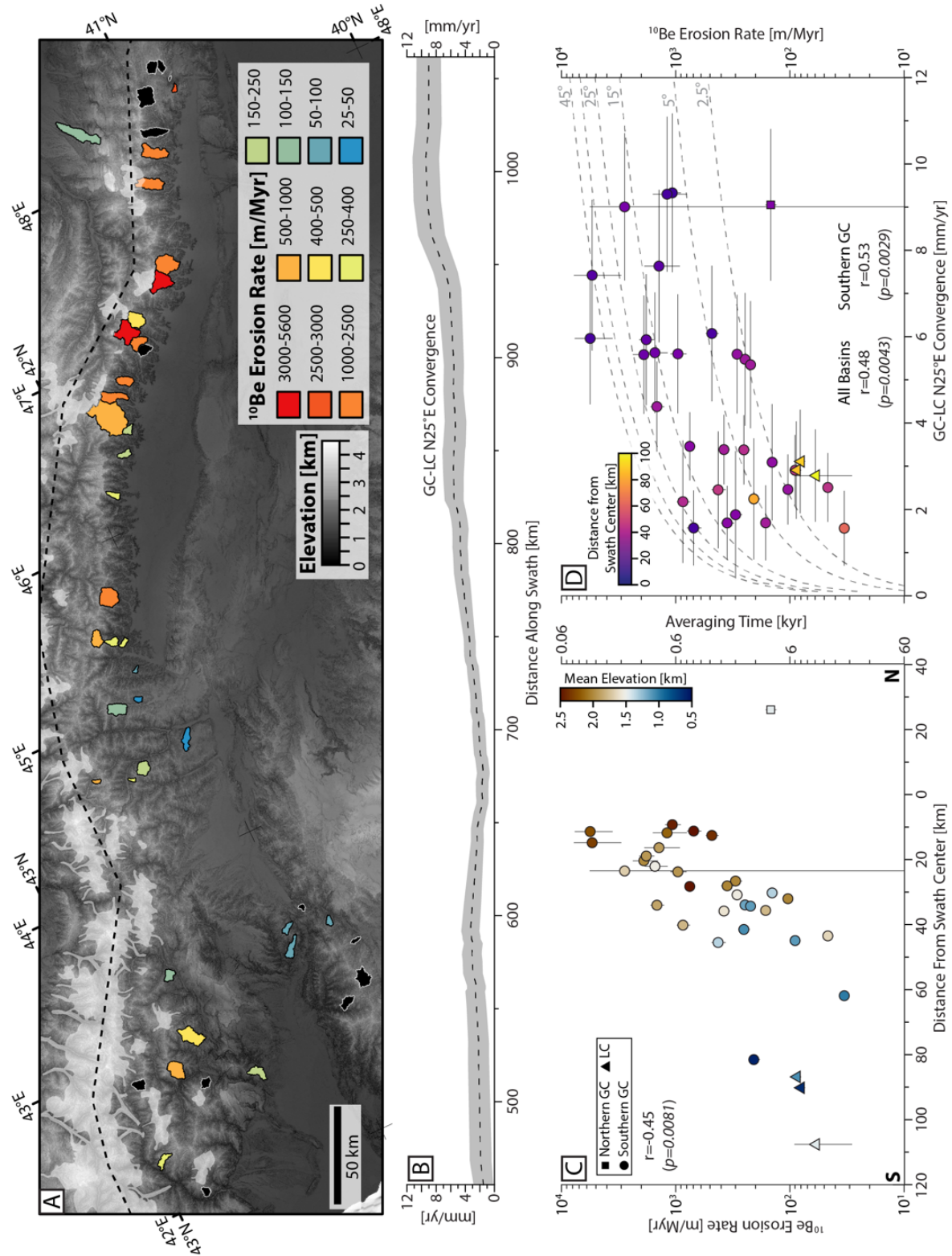
731  
 732 **Fig 5.** Hydroclimate cluster analysis. (A) Comparison of shape and mean runoff. These  
 733 two parameters were the input to the k-means cluster analysis. Squares indicate the

734 single value of shape and mean runoff used for the cluster as a whole in subsequent  
 735 analysis, see main text. An elbow plot for choosing the number of clusters is provided in  
 736 Fig. S11. Note that dashed line boundaries are meant to aid visualization and do not  
 737 define known edges of the clusters (B) Comparison of scale and mean runoff, colored  
 738 by cluster membership. Squares indicate the single value of shape and mean runoff  
 739 used for the cluster as a whole in subsequent analysis. (C) Comparison of shape and  
 740 maximum elevation within the catchment for gauged (GRDC) basins. (D) Comparison of  
 741 mean runoff and maximum elevation for the gauged and ungauged basins. Colors  
 742 represent cluster membership. For the gauged basins, these are outcomes of the k-  
 743 means clustering described in the text. For the ungauged basins, they were assigned  
 744 cluster membership by breaking this space into four quadrants (shown with the light  
 745 gray lines). For the boundary between cluster 2-3, this was tuned such that a basin  
 746 which lies within a cluster 3 gauged basin was assigned to cluster 3. (E) Spatial  
 747 distribution of clusters for both the gauged basins used to define the clusters and  
 748 ungauged basins assigned to clusters.  
 749



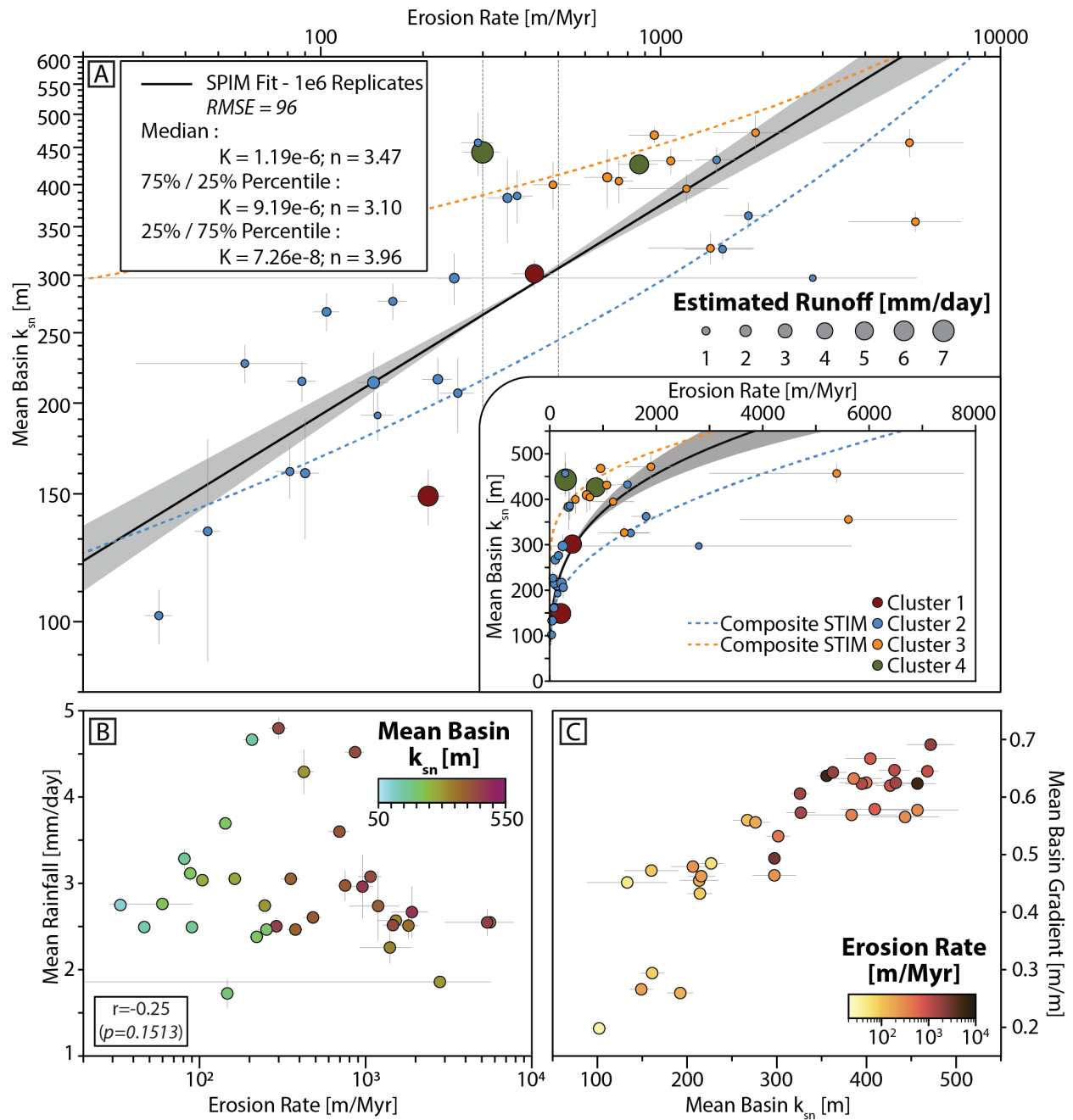
750  
 751 **Fig. 6** Results of optimization of  $k_e$  (A) and  $\tau_c$  (B) compared to distance from center of  
 752 the range (x axis) and erosion rate (scale of dots). Horizontal dotted lines represent  
 753 median by cluster and for the entire population. Shaded region indicates interquartile  
 754 range for the whole population estimates. Points are colored by cluster membership  
 755 (see Fig. 5). Comparison of the optimized values of  $k_e$  and  $\tau_c$  and lithology are  
 756 presented in Fig. S12.

757  
 758



759  
 760  
 761 **Fig 7.** (A) Cosmogenic  $^{10}\text{Be}$  erosion rates for sampled basins. Black basins indicate  
 762 unsuccessful samples (insufficient quartz yield; see Supplemental Methods for  
 763 additional discussion). White shading represents extent of LGM glaciation (Gobejishvili

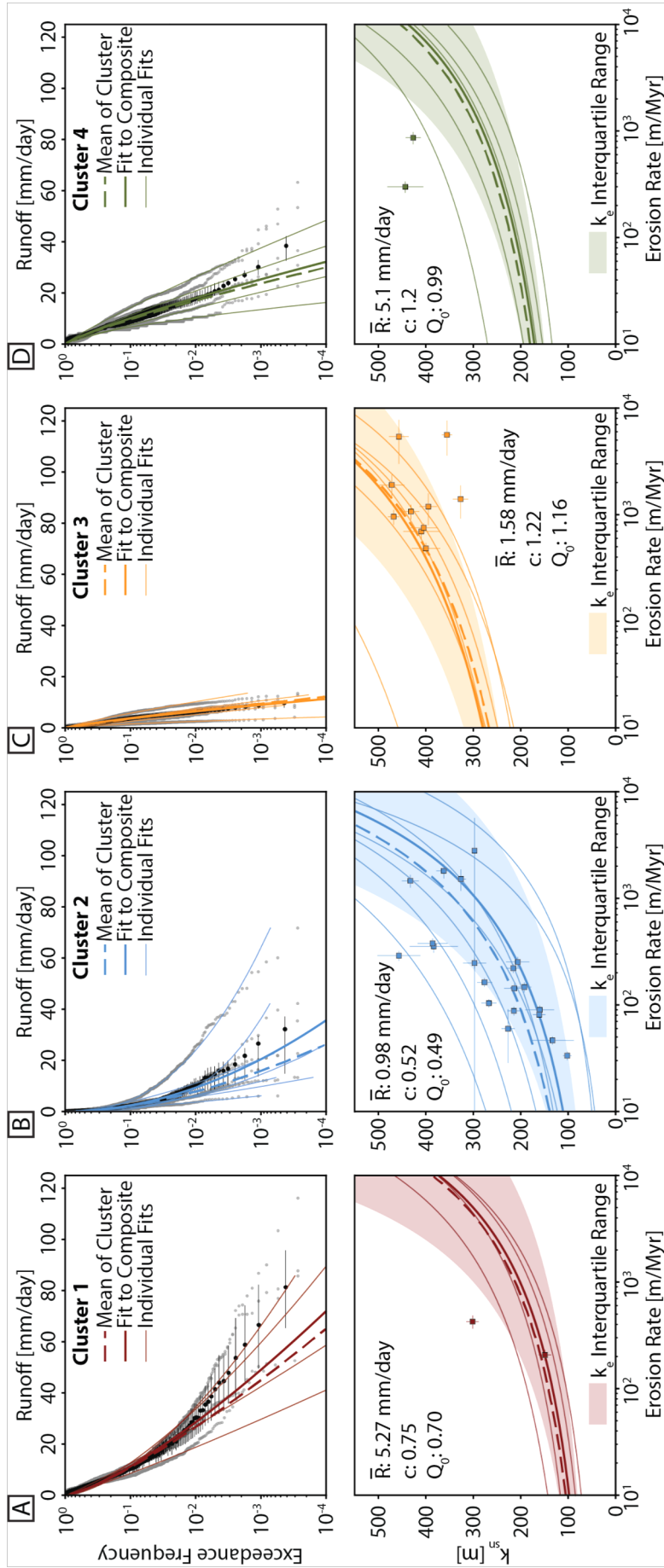
764 et al., 2011) and black dashed line marks center of swath shown in Fig. 1. (B) Estimated  
765 N25°E convergence between the GC and LC along the southern margin of the GC,  
766 identical to the red curve in Fig 1B. (C) Cosmogenic <sup>10</sup>Be erosion rates vs distance  
767 from the center of the swath (colored by mean elevation of sampled basins – Fig. S14  
768 presents a direct relationship between erosion rate and mean elevation). Pearson’s  
769 correlation coefficient (r) is shown comparing erosion rates and distance from the swath  
770 center, along with respective p value. (D) Cosmogenic <sup>10</sup>Be erosion rates vs  
771 convergence velocity (7B, colored by distance from the swath center). Contours  
772 represent the vertical component of rock uplift if convergence was accommodated along  
773 a thrust of a specified dip, these are for reference only and do not imply known  
774 structural geometries. Correlation coefficient between E and GC-LC convergence (Fig  
775 1C) is shown. Average time is calculated as the amount of time required to erode 60  
776 cm. A plot of erosion rate as a function of along-strike distance is provided in Fig. S13.  
777



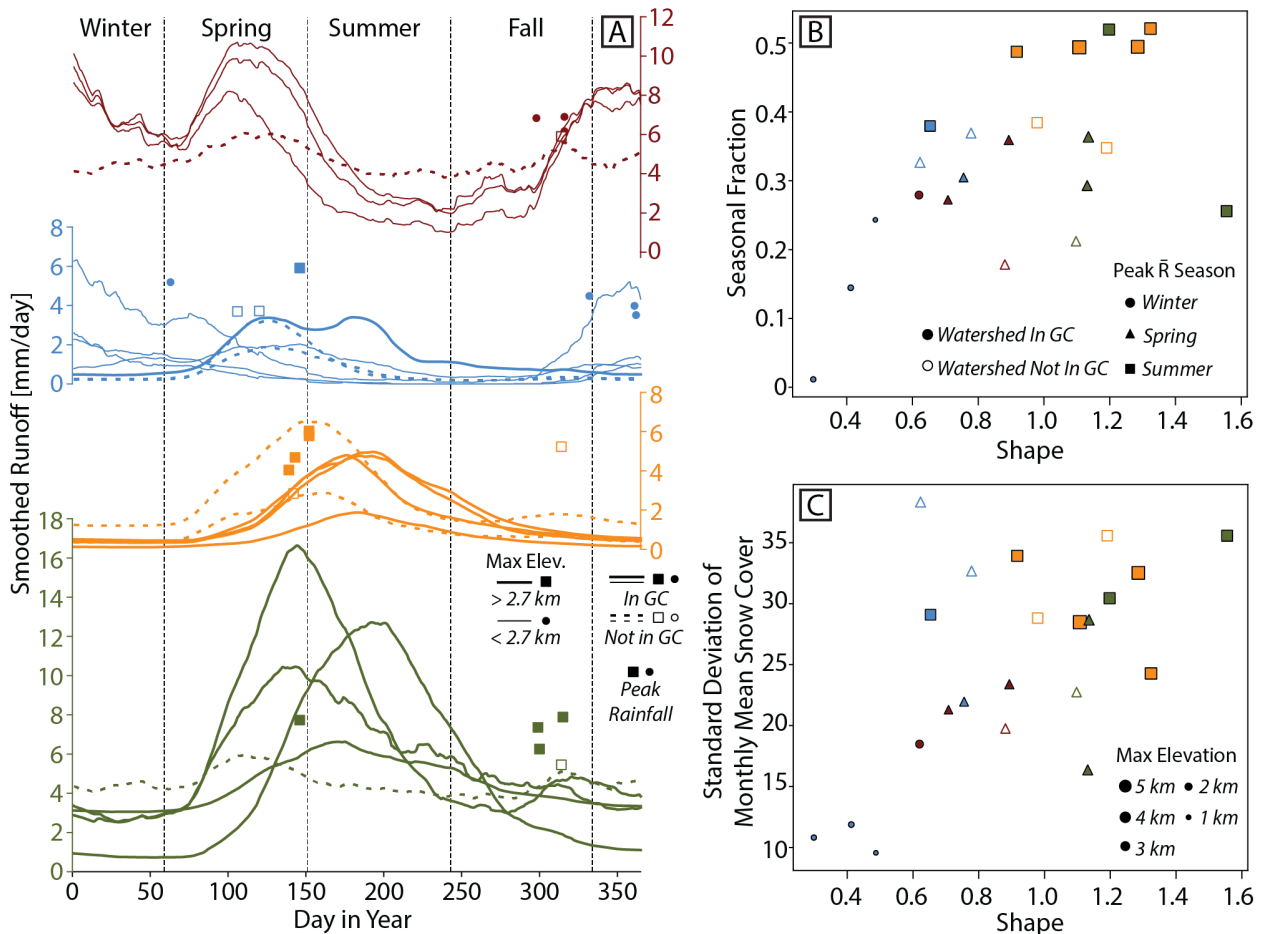
778  
779

780 **Fig. 8 (A)**  $^{10}\text{Be}$  erosion rate vs basin-averaged normalized channel steepness ( $k_{sn}$ ).  
 781 Individual basins are colored by cluster membership (see Fig. 5D) and the size of the  
 782 circles are scaled by estimated mean runoff. Curve is the best-fit power law function.  
 783 Vertical dashed lines highlight the range of  $E$  above which  $k_{sn}$  becomes largely  
 784 invariant. Inset shows same data on a linear scale. Details of the power law fit are  
 785 provided in Fig. S7. Also shown are the composite STIM relationships (Fig. 9) for  
 786 clusters 2 and 3, which represent the bulk of the data. A more direct comparison of the  
 787 degree of correspondence between the observed data and both STIM and SPIM  
 788 relationships are provided in the supplement (Fig. S15). (B)  $^{10}\text{Be}$  erosion rate vs mean  
 789 rainfall in each basin colored by  $k_{sn}$ . Pearson's correlation coefficient ( $r$ ) between

790 erosion rate and rainfall along with p-value is shown, note that this suggests non-  
791 statistically significant correlation between these variables. (C) Mean basin  $k_{sn}$   
792 compared to mean hillslope gradient, colored by  $E$ . Note that the linear relationship  
793 between  $k_{sn}$  and gradient reflects that both  $k_{sn}$  and gradient become insensitive to  
794 increases in erosion rate at  $\sim 500 \text{ m Myr}^{-1}$  (Fig. S4).  
795  
796



798 **Fig. 9** Details of runoff distributions and erosion rates for cluster 1 (A), cluster 2 (B),  
 799 cluster 3 (C), and cluster 4 (D). For all plots, the top panels display the individual runoff  
 800 distributions (gray dots) and the fits to those distributions (thin lines). Also displayed are  
 801 the implied distribution using the mean shape, scale, and runoff from each population  
 802 (thick dashed lines). Black dots represent binned composite of runoff with interquartile  
 803 range of runoff within each bin. Thick solid line is the fit to the composite distribution.  
 804 Bottom panels display implied  $E-k_{sn}$  relationships using either the individual mean  
 805 runoff, shape, and scale parameters for gauged basins (thin lines), using the population  
 806 mean (thick dashed lines), and using the fit to the composite distribution (thick solid  
 807 lines). All individual relationships use the median  $k_e$  ( $1.55e-11$ , e.g., Fig. 6), but shaded  
 808 region shows range of possible relationships using the interquartile range of  $k_e$  and the  
 809 composite distribution values. The mean runoff and composite shape and scale  
 810 parameters are reported for each cluster.  
 811  
 812



813 **Fig 10.** (A) Daily GRDC runoff, averaged over the full length of each dataset and after  
 814 applying a 31-day moving average. Dots are day of peak rainfall from TRMM processed  
 815 in the same way for the basin of interest (see Fig. S3 for rainfall time series and  
 816 difference between rainfall and runoff). Almost all basins show a peak in runoff in either  
 817 the spring or summer consistent with derivation from snowmelt. (B) Seasonal fraction of  
 818 runoff versus shape parameter for the distribution. Symbol size is scaled by maximum  
 819

820 elevation, shapes indicate the season of maximum mean runoff, and colors indicate  
821 cluster membership. GC basins (solid symbols) show a more consistent relationship  
822 than those further afield (open symbols) between seasonal fraction and shape. (C)  
823 Standard deviation in mean seasonal snow cover vs shape. Symbols are the same as in  
824 10B. Additional comparisons between fractions and both the shape and scale  
825 parameters are provided in Fig. S17.

826  
827

## 828 **References**

- 829 Allen, M.B., Jackson, J., Walker, R., 2004. Late Cenozoic reorganization of the Arabia-Eurasia  
830 collision and the comparison of short-term and long-term deformation rates. *Tectonics*  
831 23, doi:10.1029/2003TC001530-doi:10.1029/2003TC001530.
- 832 Anders, A.M., Roe, G.H., Montgomery, D.R., Hallet, B., 2008. Influence of precipitation phase on  
833 the form of mountain ranges. *Geology* 36, 479. <https://doi.org/10.1130/G24821A.1>
- 834 Avdeev, B., Niemi, N.A., 2011. Rapid Pliocene exhumation of the central Greater Caucasus  
835 constrained by low-temperature thermochronometry. *Tectonics* 30.  
836 <https://doi.org/10.1029/2010TC002808>
- 837 Balco, G., Stone, J., Lifton, N.A., Dunai, T., 2008. A complete and easily accessible means of  
838 calculating surface exposure ages or erosion rates from  $^{10}\text{Be}$  and  $^{26}\text{Al}$  measurements.  
839 *Quat. Geochronol.* 3, 174–195. <https://doi.org/10.1016/j.quageo.2007.12.001>
- 840 Berghuijs, W.R., Woods, R.A., Hrachowitz, M., 2014. A precipitation shift from snow towards  
841 rain leads to a decrease in streamflow. *Nat. Clim. Change* 4, 583–586.  
842 <https://doi.org/10.1038/nclimate2246>
- 843 Berghuijs, W.R., Woods, R.A., Hutton, C.J., Sivapalan, M., 2016. Dominant flood generating  
844 mechanisms across the United States: Flood Mechanisms Across the U.S. *Geophys. Res.*  
845 *Lett.* 43, 4382–4390. <https://doi.org/10.1002/2016GL068070>
- 846 Bierman, P.R., Nichols, K.K., 2004. Rock to sediment - slope to sea with  $^{10}\text{Be}$  - rates of  
847 landscape change. *Annu. Rev. Earth Planet. Sci.* 32, 215–235.
- 848 Bookhagen, B., Burbank, D., 2006. Topography, relief, and TRMM-derived rainfall variations  
849 along the Himalaya. *Geophys. Res. Lett.* 33, L08405–L08405.  
850 <https://doi.org/10.1029/2006GL026037>
- 851 Campforts, B., Vanacker, V., Herman, F., Vanmaercke, M., Schwanghart, W., Tenorio, G.E.,  
852 Willems, P., Govers, G., 2020. Parameterization of river incision models requires  
853 accounting for environmental heterogeneity: insights from the tropical Andes. *Earth*  
854 *Surf. Dyn.* 8, 447–470. <https://doi.org/10.5194/esurf-8-447-2020>
- 855 Cowgill, E., Forte, A.M., Niemi, N.A., Avdeev, B., Tye, A.R., Trexler, C.C., Javakishvirli, Z., Elashvili,  
856 M., Godoladze, T., 2016. Relict basin closure and crustal shortening budgets during  
857 continental collision: An example from Caucasus sediment provenance. *Tectonics* 35,  
858 2918–2947. <https://doi.org/10.1002/2016TC004295>
- 859 Deal, E., Braun, J., Botter, G., 2018. Understanding the Role of Rainfall and Hydrology in  
860 Determining Fluvial Erosion Efficiency. *J. Geophys. Res. Earth Surf.* 123, 744–778.  
861 <https://doi.org/10.1002/2017JF004393>

862 DiBiase, R.A., Whipple, K.X., 2011. The influence of erosion thresholds and runoff variability on  
863 the relationships among topography, climate, and erosion rate. *J. Geophys. Res.* 116.  
864 <https://doi.org/10.1029/2011JF002095>

865 DiBiase, R.A., Whipple, K.X., Heimsath, A.M., Ouimet, W.B., 2010. Landscape form and  
866 millennial erosion rates in the San Gabriel Mountains, CA. *Earth Planet. Sci. Lett.* 289,  
867 134–144.

868 Eckhardt, K., 2008. A comparison of baseflow indices, which were calculated with seven  
869 different baseflow separation methods. *J. Hydrol.* 352, 168–173.  
870 <https://doi.org/10.1016/j.jhydrol.2008.01.005>

871 Ferrier, K.L., Huppert, K.L., Perron, J.T., 2013. Climatic control of bedrock river incision. *Nature*  
872 496, 206–209. <https://doi.org/10.1038/nature11982>

873 Fisher, G.B., Bookhagen, B., Amos, C.B., 2013. Channel planform geometry and slopes from  
874 freely available high-spatial resolution imagery and DEM fusion: Implications for channel  
875 width scalings, erosion proxies, and fluvial signatures in tectonically active landscapes.  
876 *Geomorphology* 194, 46–56. <https://doi.org/10.1016/j.geomorph.2013.04.011>

877 Forte, A.M., 2021. Lithologic compilation of basins sampled for cosmogenic <sup>10</sup>Be in the Greater  
878 Caucasus Mountains.

879 Forte, A.M., Cowgill, E., Murtuzayev, I., Kangarli, T., Stoica, M., 2013. Structural geometries and  
880 magnitude of shortening in the eastern Kura fold-thrust belt, Azerbaijan: Implications  
881 for the development of the Greater Caucasus Mountains. *Tectonics* 32.  
882 <https://doi.org/10.1002/tect.20032>

883 Forte, A.M., Cowgill, E., Whipple, K.X., 2014. Transition from a singly vergent to doubly vergent  
884 wedge in a young orogen: The Greater Caucasus. *Tectonics* 33, 2077–2101.  
885 <https://doi.org/10.1002/2014TC003651>

886 Forte, A.M., Whipple, K.X., 2019. Short communication : The Topographic Analysis Kit (TAK) for  
887 TopoToolbox. *Earth Surf. Dyn.* 7, 87–95. <https://doi.org/10.5194/esurf-7-87-2019>

888 Forte, A.M., Whipple, K.X., Bookhagen, B., Rossi, M.W., 2016. Decoupling of modern shortening  
889 rates, climate, and topography in the Caucasus. *Earth Planet. Sci. Lett.* 449, 282–294.  
890 <https://doi.org/10.1016/j.epsl.2016.06.013>

891 Forte, A.M., Whipple, K.X., Cowgill, E., 2015. Drainage network reveals patterns and history of  
892 active deformation in the eastern Greater Caucasus. *Geosphere* 11.  
893 <https://doi.org/10.1130/GES01121.1>

894 Gallen, S.F., Fernández-Blanco, D., 2021. A New Data-driven Bayesian Inversion of Fluvial  
895 Topography Clarifies the Tectonic History of the Corinth Rift and Reveals a Channel  
896 Steepness Threshold. *J. Geophys. Res. Earth Surf.*  
897 <https://doi.org/10.1029/2020JF005651>

898 Gobejishvili, R., Lomidze, N., Tielidze, L., van der Meer, J.J.M., 2011. Late Pleistocene (Würmian)  
899 Glaciations of the Caucasus, in: Ehlers, J., Gibbard, P.L., Hughes, P.D. (Eds.), *Quaternary*  
900 *Glaciations - Extent and Chronology*. Elsevier, Amsterdam, pp. 141–147.

901 Hall, D.K., Riggs, G.A., Salomonson, V.V., 2006. MODIS/Terra Snow Cover 5-Min L2 Swath 500m.  
902 Version 5. NASA National Snow and Ice Data Center Distributed Archive Center, Boulder,  
903 CO.

904 Harel, M.A., Mudd, S.M., Attal, M., 2016. Global analysis of the stream power law parameters  
905 based on worldwide 10Be denudation rates. *Geomorphology* 268, 184–196.  
906 <https://doi.org/10.1016/j.geomorph.2016.05.035>

907 Huffman, G.J., Adler, R.F., Bolvin, D.T., Gu, G., Nelkin, E.J., Bowman, K.P., Hong, Y., Stockler, E.F.,  
908 Wolff, D.B., 2007. The TRMM multisatellite precipitation analysis (TMPA): Quasi-global,  
909 multiyear, combined-sensor precipitation estimate at fine scales. *J. Hydrometeorol.* 8,  
910 38–55. <https://doi.org/10.1175/JHM560.1>

911 Johnson, J.P.L., Whipple, K.X., Sklar, L., 2010. Contrasting bedrock incision rates from snowmelt  
912 and flash floods in the Henry Mountains, Utah. *Geol. Soc. Am. Bull.* 122, 1600–1615.

913 Kadirov, F., Floyd, M., Alizadeh, A., Guliev, I., Reilinger, R., Kuleli, S., King, R., Toksoz, M.N., 2012.  
914 Kinematics of the eastern Caucasus near Baku, Azerbaijan. *Nat. Hazards* 63, 997–1006.

915 Kirby, E., Whipple, K.X., 2012. Expression of active tectonics in erosional landscapes. *J. Struct.*  
916 *Geol.* 44, 54–75.

917 Kuchment, L.S., Gelfan, A.N., Demidov, V.N., 2010. A spatial model of snowmelt-rainfall runoff  
918 formation of the mountain river (by the example of the Upper Kuban River). *Russ.*  
919 *Meteorol. Hydrol.* 35, 842–850. <https://doi.org/10.3103/S1068373910120083>

920 Lague, D., 2014. The stream power river incision model: evidence, theory and beyond. *Earth*  
921 *Surf. Process. Landf.* 39, 38–61. <https://doi.org/10.1002/esp.3462>

922 Lague, D., Hovius, N., Davy, P., 2005. Discharge, discharge variability, and the bedrock channel  
923 profile. *J. Geophys. Res.* 110, F04006–F04006. <https://doi.org/10.1029/2004JF000259>

924 Mifsud, C., Fujioka, T., Fink, D., 2013. Extraction and purification of quartz in rock using hot  
925 phosphoric acid for in situ cosmogenic exposure dating. *Nucl. Instrum. Methods Phys.*  
926 *Res. B* 294, 203–207. <https://doi.org/10.1016/j.nimb.2012.08.037>

927 Mosar, J., Kangarli, T., Bochud, M., Glasmacher, U.A., Rast, A., Brunet, M.-F., Sosson, M., 2010.  
928 Cenozoic-Recent tectonics and uplift in the Greater Caucasus: a perspective from  
929 Azerbaijan, in: Sosson, M., Kaymakci, N., Stephenson, R.A., Bergerat, F., Starostenko, V.I.  
930 (Eds.), *Sedimentary Basin Tectonics from the Black Sea and Caucasus to the Arabian*  
931 *Platform*. Geological Society, London, pp. 261–280.

932 Portenga, E.W., Bierman, P.R., 2011. Understanding Earth’s eroding surface with 10Be. *GSA*  
933 *Today* 21, 4–10. <https://doi.org/10.1130/G1111A.1>

934 Reilinger, R., McClusky, S., Vernant, P., Lawrence, S., Ergintav, S., Cakmak, R., Ozener, H.,  
935 Kadirov, F., Guliev, I., Stepanyan, R., Nadariya, M., Hahubia, G., Mahmoud, S., Sakr, K.,  
936 ArRajehi, A., Paradissis, D., Al-Aydrus, A., Prilepin, M., Guseva, T., Evren, E., Dmitrotsa,  
937 A., Filikov, S.V., Gomez, F., Al-Ghazzi, R., Karam, G., 2006. GPS constraints on continental  
938 deformation in the Africa-Arabia-Eurasia continental collision zone and implications for  
939 the dynamics of plate interactions. *J. Geophys. Res.* 111, doi:10.1029/2005JB004051-  
940 doi:10.1029/2005JB004051.

941 Rets, E.P., Dzhamalov, R.G., Kireeva, M.B., Frolova, N.L., Durmanov, I.N., Telegina, A.A.,  
942 Telegina, E.A., Grigoriev, V.Yu., 2018. RECENT TRENDS OF RIVER RUNOFF IN THE NORTH  
943 CAUCASUS. *Geogr. Environ. Sustain.* 11, 61–70. [https://doi.org/10.24057/2071-9388-  
944 2018-11-3-61-70](https://doi.org/10.24057/2071-9388-2018-11-3-61-70)

945 Rossi, M.W., Anderson, R.S., Anderson, S.P., Tucker, G.E., 2020. Orographic Controls on Subdaily  
946 Rainfall Statistics and Flood Frequency in the Colorado Front Range, USA. *Geophys. Res.*  
947 *Lett.* 47. <https://doi.org/10.1029/2019GL085086>

948 Rossi, M.W., Whipple, K.X., Vivoni, E.R., 2016. Precipitation and evapotranspiration controls on  
949 event-scale runoff variability in the contiguous United States and Puerto Rico. *J.*  
950 *Geophys. Res.* 121. <https://doi.org/10.1002/2015JF003446>  
951 Schaeffli, B., Rinaldo, A., Botter, G., 2013. Analytic probability distributions for snow-dominated  
952 streamflow: Snow-Dominated Streamflow Pdfs. *Water Resour. Res.* 49, 2701–2713.  
953 <https://doi.org/10.1002/wrcr.20234>  
954 Scherler, D., Bookhagen, B., Strecker, M.R., 2014. Tectonic control on 10 Be-derived erosion  
955 rates in the Garhwal. *J. Geophys. Res. Earth Surf.* 119, 83–105.  
956 <https://doi.org/10.1002/2013JF002955>  
957 Scherler, D., DiBiase, R.A., Fisher, G.B., Avouac, J.-P., 2017. Testing monsoonal controls on  
958 bedrock river incision in the Himalaya and Eastern Tibet with a stochastic-threshold  
959 stream power model. *J. Geophys. Res. Earth Surf.* 122, 1389–1429.  
960 <https://doi.org/10.1002/2016JF004011>  
961 Schwanghart, W., Scherler, D., 2014. Short Communication: TopoToolbox 2 - MATLAB based  
962 software for topographic analysis and modeling in Earth surface sciences. *Earth Surf.*  
963 *Dyn.* 2, 1–7. <https://doi.org/10.5194/esurf-2-1-2014>  
964 Shobe, C.M., Tucker, G.E., Rossi, M.W., 2018. Variable-Threshold Behavior in Rivers Arising  
965 From Hillslope-Derived Blocks. *J. Geophys. Res. Earth Surf.* 123, 1931–1957.  
966 <https://doi.org/10.1029/2017JF004575>  
967 Sloto, R.A., Crouse, M.Y., 1996. HYSEP: A Computer Program for Streamflow Hydrograph  
968 Separation and Analysis. <https://doi.org/10.3133/wri964040>  
969 Sokhadze, G., Floyd, M., Godoladze, T., King, R., Cowgill, E.S., Javakhishvili, Z., Hahubia, G.,  
970 Reilinger, R., 2018. Active convergence between the Lesser and Greater Caucasus in  
971 Georgia: Constraints on the tectonic evolution of the Lesser–Greater Caucasus  
972 continental collision. *Earth Planet. Sci. Lett.* 481, 154–161.  
973 <https://doi.org/10.1016/j.epsl.2017.10.007>  
974 Stone, J.O., 2000. Air pressure and cosmogenic isotope production. *J. Geophys. Res. Solid Earth*  
975 105, 23753–23759. <https://doi.org/10.1029/2000JB900181>  
976 Sutcliffe, J.V., Farquharson, F.A.K., Tate, E.L., Folwell, S.S., 2008. Flood regimes in the Southern  
977 Caucasus: the influence of precipitation on mean annual floods and frequency curves.  
978 *Hydrol. Res.* 39, 385–401. <https://doi.org/10.2166/nh.2008.025>  
979 Trexler, C.C., Cowgill, E., Spencer, J.Q.G., Godoladze, T., 2020. Rate of active shortening across  
980 the southern thrust front of the Greater Caucasus in western Georgia from kinematic  
981 modeling of folded river terraces above a listric thrust. *Earth Planet. Sci. Lett.* 544,  
982 116362. <https://doi.org/10.1016/j.epsl.2020.116362>  
983 Tucker, G.E., 2004. Drainage basin sensitivity to tectonic and climatic forcing: Implications of a  
984 stochastic model for the role of entrainment and erosion thresholds. *Earth Surf. Process.*  
985 *Landf.* 29, 185–204. <https://doi.org/10.1002/esp.1020>  
986 Vasil'chuk, Yu.K., Rets, E.P., Chizhova, Ju.N., Tokarev, I.V., Frolova, N.L., Budantseva, N.A.,  
987 Kireeva, M.B., Loshakova, N.A., 2016. Hydrograph separation of the Dzhankuat River,  
988 North Caucasus, with the use of isotope methods. *Water Resour.* 43, 847–861.  
989 <https://doi.org/10.1134/S0097807816060087>  
990 Verdiev, R.G., 2009. Computation and prediction of the flood runoff of the Eastern Caucasus  
991 Rivers. *Russ. Meteorol. Hydrol.* 34, 46–50.

992 Vezzoli, G., Garzanti, E., Limonta, M., Radeff, G., 2020. Focused erosion at the core of the  
 993 Greater Caucasus: Sediment generation and dispersal from Mt. Elbrus to the Caspian  
 994 Sea. *Earth-Sci. Rev.* 200, 102987. <https://doi.org/10.1016/j.earscirev.2019.102987>  
 995 Vezzoli, G., Garzanti, E., Vincent, S.J., Ando, S., Carter, A., Resentini, A., 2014. Tracking sediment  
 996 provenance and erosional evolution of the western Greater Caucasus. *Earth Surf.*  
 997 *Process. Landf.* <https://doi.org/10.1002/esp.3567>  
 998 Vincent, S.J., Carter, A., Lavrishchev, A., Rice, S.P., Barabadze, T.G., Hovius, N., 2011. The  
 999 exhumation of the western Greater Caucasus: a thermochronometric study. *Geol. Mag.*  
 1000 148, 1–21. <https://doi.org/10.1017/S0016756810000257>  
 1001 Vincent, S.J., Somin, M.L., Carter, A., Vezzoli, G., Fox, M., Vautravers, B., 2020. Testing Models  
 1002 of Cenozoic Exhumation in the Western Greater Caucasus. *Tectonics* 39.  
 1003 <https://doi.org/10.1029/2018TC005451>  
 1004 Whipple, K.X., 2009. The influence of climate on the tectonic evolution of mountain belts. *Nat.*  
 1005 *Geosci.* 2, 97–104.  
 1006 Whipple, K.X., DiBiase, R.A., Crosby, B., Johnson, J.P.L., 2022. Bedrock Rivers, in: Shroder, J.  
 1007 (Jack) F. (Ed.), *Treatise on Geomorphology (Second Edition)*. Academic Press, Oxford, pp.  
 1008 865–903. <https://doi.org/10.1016/B978-0-12-818234-5.00101-2>  
 1009 Whipple, K.X., Meade, B., 2004. Controls on the strength of coupling among climate, erosion,  
 1010 and deformation in two-sided, frictional orogenic wedges at steady state. *J. Geophys.*  
 1011 *Res.* 109, F01011–F01011. <https://doi.org/10.1029/2003JF000019>  
 1012 Willett, S.D., 1999. Orogeny and orography: The effects of erosion on the structure of mountain  
 1013 belts. *J. Geophys. Res.* 104, 28,928-957,981.  
 1014 Wilson, P.S., Toumi, R., 2005. A fundamental probability distribution for heavy rainfall.  
 1015 *Geophys. Res. Lett.* 32, n/a-n/a. <https://doi.org/10.1029/2005GL022465>  
 1016 Wulf, H., Bookhagen, B., Scherler, D., 2016. Differentiating between rain, snow, and glacier  
 1017 contributions to river discharge in the western Himalaya using remote-sensing data and  
 1018 distributed hydrologic modeling. *Adv. Water Resour.* 88, 152–169.  
 1019 <https://doi.org/10.1016/j.advwatres.2015.12.004>  
 1020